

ATOMS: ALMA Three-millimeter Observations of Massive Star-forming regions -XIII. Ongoing triggered star formation within clump-fed scenario found in the massive ($\sim 1500 M_{\odot}$) clump

Siju Zhang,^{1*} Ke Wang,^{1†} Tie Liu,^{2,3} Annie Zavagno,^{4,5} Mika Juvela,⁶ Hongli Liu,⁷ Anandmayee Tej,⁸ Amelia M. Stutz,⁹ Shanghuo Li,¹⁰ Leonardo Bronfman,¹¹ Qizhou Zhang,¹² Paul F. Goldsmith,¹³ Chang Won Lee,^{14,15} Enrique Vázquez-Semadeni,¹⁶ Ken'ichi Tatematsu,^{17,18} Wenyu Jiao,^{1,19} Fengwei Xu,^{1,19} Chao Wang,^{1,19} Jian-Wen Zhou^{20,21}

Affiliations are listed at the end of the paper

Accepted 2022 December 28. Received 2022 December 28; in original form 2022 June 15

ABSTRACT

Whether ionization feedback triggers the formation of massive stars is highly debated. Using ALMA 3 mm observations with a spatial resolution of ~ 0.05 pc and a mass sensitivity of $1.1 M_{\odot} \text{ beam}^{-1}$ at 20 K, we investigate the star formation and gas flow structures within the ionizing feedback-driven structure, a clump-scale massive ($\gtrsim 1500 M_{\odot}$) bright-rimmed cloud (BRC) associated with IRAS 18290–0924. This BRC is bound only if external compression from ionized gas is considered. A small-scale ($\lesssim 1$ pc) age sequence along the direction of ionizing radiation is revealed for the embedded cores and protostars, which suggests triggered star formation via radiation-driven implosion (RDI). Furthermore, filamentary gas structures converge towards the cores located in the BRC's center, indicating that these filaments are fueling mass towards cores. The local core-scale mass infall rate derived from $\text{H}^{13}\text{CO}^+ J = 1 - 0$ blue profile is of the same order of magnitude as the filamentary mass inflow rate, approximately $1 M_{\odot} \text{ kyr}^{-1}$. A photodissociation region (PDR) covering the irradiated clump surface is detected in several molecules, such as CCH, HCO^+ , and CS whereas the spatial distribution stratification of these molecules is indistinct. CCH spectra of the PDR possibly indicate a photoevaporation flow leaving the clump surface with a projected velocity of $\sim 2 \text{ km s}^{-1}$. Our new observations show that RDI accompanied by a clump-fed process is operating in this massive BRC. Whether this combined process works in other massive BRCs is worth exploring with dedicated surveys.

Key words: stars: formation – stars: kinematics and dynamics; ISM: H II regions – ISM: clouds – ISM: photodissociation region (PDR)

1 INTRODUCTION

How massive stars gain their mass during formation is a longstanding problem (Bonnell et al. 2001; McKee & Tan 2003; Zinnecker & Yorke 2007; Krumholz et al. 2009). Motte et al. (2018) highlighted the key roles of global hierarchical collapse and clump-fed process in high-mass star formation (HMSF). Padoan et al. (2020) proposed that the large-scale and converging inertial flows in supersonic-turbulence environment are assembled to form clumps and cores as a first step toward formation of massive stars. The intricate interplay between birthplaces and environment in these scenarios shows that the environmental factors beyond the core scale (~ 0.1 pc) are crucial to understand HMSF.

One of the widely discussed environmental factors is the feedback from external ionized (H II) regions. The close associations between H II regions and other HMSF sites have been well discussed in a number of works, for example by Thompson et al. (2012) for

UCH II regions, Kendrew et al. (2016) for massive cold clumps, Palmeirim et al. (2017) for young stellar objects (YSOs), and Zhang et al. (2020, 2021) for high-mass starless clumps. However, whether ionization feedback induces or suppresses formation of the next-generation stars is highly debatable and is potentially linked to the key questions of star formation efficiency (SFE) of the Milky Way (Geen et al. 2017; Fukushima et al. 2020; González-Samaniego & Vázquez-Semadeni 2020). The mechanical and radiative feedback of ionized regions could induce star formation mainly via two mechanisms: (1) Collect and collapse: A massive molecular shell is collected between an ionization front (IF) and a shock front (SF), and then this shell fragments and collapses to form stars (Whitworth et al. 1994; Deharveng et al. 2005; Zavagno et al. 2007; Liu et al. 2015, 2016, 2017a). (2) Radiation-driven implosion (RDI, Bertoldi 1989): The surface of a pre-existing molecular clump is ionized by the UV radiation from nearby OB stars, plus the pre-existing ionized gas of the H II region that is jammed on the clump surface, forming an over-pressure ionized boundary layer (IBL). This IBL drives a photoevaporation flow leaving clump surface and a shock penetrating

* E-mail: sijuzhangastro@gmail.com

† E-mail: kwang.astro@pku.edu.cn

the clump interior, compressing the clump and inducing its collapse for future star formation (Lefloch & Lazareff 1994).

The bright-rimmed clouds (BRCs), with the bright rim generally tracing the IBL that can be detected in free-free and/or recombination line emission, are candidate sites of the RDI mechanism being at work. BRCs were first systematically searched by Sugitani, Fukui and Ogura (so called “SFO” BRCs, Sugitani et al. 1991; Sugitani & Ogura 1994) in the surrounding of the optically visible H II regions (e.g. Sharpless 1959) with a size larger than 60′, which biases their selected BRCs to the near distances and thus to the low- or intermediate-mass regime. Figure 1 shows the mass distribution for BRCs and other objects that may relate RDI, such as cometary globules (CGs) and pillars, collected by us from a number of observational and modelling works (200+ sources in 50+ papers, see Appendix Table A1). In the figure, the “SFO”, “CG”, and “individual” represent the BRCs catalogued by Sugitani, Fukui and Ogura, the CGs catalogued by Maheswar & Bhatt (2008), and other individual case studies not included in the two catalogues, respectively. Although it is impractical to list all related works, we see that not only “SFO” BRCs are mainly in low- to intermediate-mass regime, but also for other potentially RDI-driven objects in many follow-up works.

This observed regime may be due to both observational biases and physical natures. On the one hand, nearby bright H II regions attract more attention in the previous selection of BRCs, leading to the bias toward the low- to intermediate-mass BRCs. On the other hand, a large fraction of clump mass are being peeled off by photoionization, dissociation, and evaporation. In addition, the turbulent nature of the massive clumps could also assist in forming less massive BRCs. Turbulent HMSF regions prefer to form low-mass pillar-like structures when strong UV radiation penetrates low-density regions in the turbulent clouds (Gritschneider et al. 2009a,b).

Actually, massive BRCs with a mass more than few thousand solar masses can be found in our Galaxy, such as those selected by us from the ALMAGAL survey in Fig. 1. The ALMAGAL (ALMA Evolutionary study of High Mass Protocluster Formation in the Galaxy, Project ID: 2019.1.00195.L) targets at using ALMA to survey nearly 1000 dense ($\gtrsim 0.1 \text{ g cm}^{-2}$) and massive ($\gtrsim 500 M_{\odot}$) Hi-GAL clumps (Elia et al. 2017) within distance $\lesssim 7.5 \text{ kpc}$. A check on $4' \times 4'$ environment of 860 ALMAGAL clumps using the *Spitzer* 24/8.0/4.5 μm RGB image reveals that a number of ALMAGAL clumps are close to the extended 24 μm emission region. The two example maps are shown in Appendix Figs. A1 and A2. The extended 24 μm emission of hot dust strongly correlates with the radio free-free emission of H II region, as revealed by Ingallinera et al. (2014) and Makai et al. (2017). Moreover, this correlation forms the basis that mid-infrared images such as *Spitzer* 24/8.0/4.5 μm RGB images can be used for identification of bubble-like H II regions (Churchwell et al. 2006; Anderson et al. 2014). Some of H II-region-nearby ALMAGAL clumps present a convex shape pointing to the inner of extended 24 μm emission region and thus show a BRC morphology (“ALMAGAL BRC” in Fig. 1). It is worth noting that these massive BRCs are not studied yet regarding RDI. Some ALMAGAL clumps are simply located on the edge of H II regions and do not present a prominent convex shape (so called “ALMAGAL H II” in Fig. 1).

The existence of ALMAGAL BRCs in Fig. 1 raises the questions on whether and how RDI works in massive BRCs, which have not been well explored yet by existing observations. The few BRCs (Ortega et al. 2016; Schneider et al. 2016) with clump mass $M_{\text{clp}} \gtrsim 1000 M_{\odot}$ which belong to “individual” type in Fig. 1 have been only studied with single-dish radio telescopes; hence, because of their far distances of several kpcs, the small scales of $\lesssim 0.1 \text{ pc}$ representative of the core scale remain inaccessible in this mass regime. In this work,

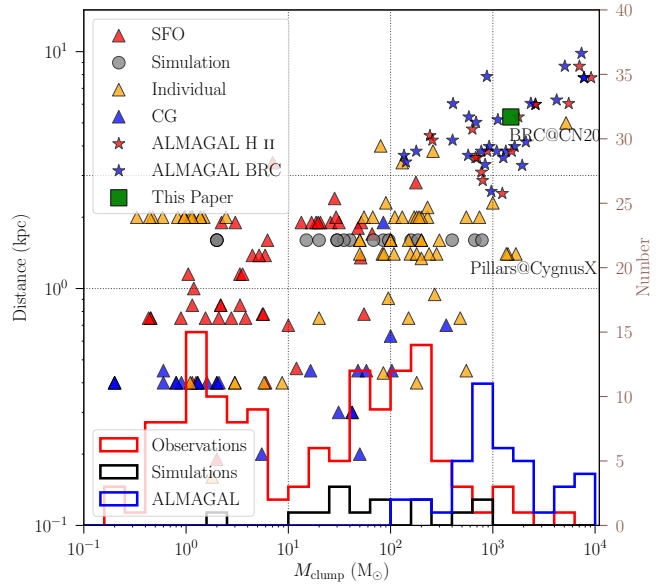


Figure 1. Summary of the published studies about RDI. The meanings of “SFO”, “CG”, “individual”, “ALMAGAL H II”, and “ALMAGAL BRC” can be found in Sect. 1. “BRC@CN20” (Ortega et al. 2016) and “Pillars@CygnusX” (Schneider et al. 2016) highlight the two single-dish observations which have the clump mass of $> 1000 M_{\odot}$. The histograms show the number distributions of different types of studies. Dashed grids mark the mass of 10, 10^2 , and $10^3 M_{\odot}$ and the distances of 1 and 3 kpc. The mass and distance of ALMAGAL sources are taken from Urquhart et al. (2018). The mass for other sources is mainly derived from either continuum emission of dust or line emission of molecules, e.g. ^{13}CO and C^{18}O . Therefore, the uncertainty of the mass estimation for all sources in the figure is difficult to unify, and thus should be cautioned. The distance for simulation work is assumed to be the averaged distance of the entire sample because many simulations do not set the distance. The detailed information for the whole sample in this figure is in Appendix A.

we present a comprehensive, pilot study of the clump-scale massive ($\sim 1500 M_{\odot}$) bright-rimmed cloud IRAS 18290–0924 (I18290 hereafter). Using ALMA high-resolution data, we demonstrate that the radiation-driven implosion is at work in a framework of clump-fed scenario for this massive BRC by investigating in great detail star formation therein and its gas kinematics. The results of this pilot work open a new window for studying details of the radiation-driven implosion in massive BRCs.

2 MAIN DATA

I18290 was observed by the ALMA project ATOMS (ALMA Three-millimeter Observations of Massive Star-forming regions, Project ID: 2019.1.00685.S; PI: Tie Liu, Liu et al. 2020a), which aims to survey 146 massive star-forming clumps (Faúndez et al. 2004) at ALMA Band 3 using single-point mapping. The combined main array and ACA 7 m data result in a continuum sensitivity of $0.08 \text{ mJy beam}^{-1}$ and a spatial resolution of $\sim 2''$ ($\sim 0.05 \text{ pc}$ at $D = 5.34 \text{ kpc}$, see the next section), with an imaged field radius of $44''$ (down to 20% primary beam response). More details about the ALMA data can be found in Appendix B1 and ATOMS papers (e.g. Liu et al. 2020b, 2021a, 2022a,b). Besides, a series of supplementary data, including single-dish CO maps, the Very Large Array (VLA) 20 cm continuum maps and NH_3 cube, the *Herschel* column density

and dust temperature maps, and the *Spitzer* images are described in Appendix B2.

3 BRC ENVIRONMENT AND GLOBAL STATUS

3.1 Environment

The environment of I18290 is shown in Fig. 2. A rim bright at 8 μm , mainly tracing the mid-infrared emission of the aromatic infrared bands of polycyclic aromatic hydrocarbons (PAHs) in photodissociation region (PDR), extends from the ATLASGAL 870 μm central clump (Urquhart et al. 2018) to the north and south. The 8- μm rim extracted by the algorithm Filfinder (Koch & Rosolowsky 2015) has a length of ~ 10 pc, a beam-deconvolved FWHM width of ~ 0.36 pc, and a mean column density N_{H_2} from *Herschel* maps of $\sim 2 \times 10^{22} \text{ cm}^{-2}$. The total mass of the 10-pc rim excluding the central clump derived from the *Herschel* N_{H_2} map is $\sim 1100 M_{\odot}$. The details of rim extraction and mass calculations can be found in Appendix C1. An IBL covering nearly half of the clump surface is traced by 20 cm free-free emission shown in Fig. 2.

I18290 is located in the giant molecular complex (GMC) G23.3–0.3 which harbours several H II regions and supernova remnants (SNRs) at a distance around 4 to 5 kpc (Su et al. 2014; Messineo et al. 2014). The rim points to the geometric center of an OB cluster with more than 10 OB stars (regions REG7 and GLIMPSE09 in Fig. 8 of Messineo et al. 2014), with a projected separation of $\sim 30'$ (45 pc). Therefore, we propose that these OB stars are potential exciting sources for the rim.

3.2 Clump under external compression

The kinematic distance and corresponding SED-resulted clump mass M_{clp} derived by Urquhart et al. (2018) are 5.34 kpc and $1420 M_{\odot}$, respectively, consistent with other studies (Lu et al. 2014; Mège et al. 2021). Our independent calculations using $^{13}\text{CO } J = 1 - 0$ transition give $M_{\text{clp}} \simeq 1450 M_{\odot}$ with an error $\sim 30\%$ (details in Appendix D1). Considering errors from abundance, excitation temperature T_{ex} , and beam size, the ^{13}CO -derived M_{clp} is in good agreement with the continuum-derived M_{clp} . The total mass of the clump and the rim is $\sim 2500 M_{\odot}$.

Virial status is key to understanding the state of equilibrium for the clump, especially if the clump is deeply influenced by the external compression from IBL. The compression is confirmed by the remarkably steeper radial profile of cold dust emission for the side facing the ionizing radiation shown in Panel a of Fig. 2, similar to the RCW 120 bubble shell revealed by Zavagno et al. (2020). The power-law fittings to the ATLASGAL 870 μm intensity profiles (Schuller et al. 2009) of I18290 yield the power-law indexes of -1.34 ± 0.3 and -0.55 ± 0.1 for the irradiated and non-irradiated sides, respectively.

We first estimate the external pressure P_{ex} exerted by the ionized region which is composed of two parts: (1) the ram pressure from the sonic ionized flow in the form of $P_{\text{ram}} = \rho_i c_i^2$ and (2) the bulk pressure of the IBL via $P_{\text{IBL}} = \rho_i c_i^2$ (Lefloch & Lazareff 1994; Morgan et al. 2004; Haworth et al. 2012), where $c_i = \sqrt{2.2 k_B T_e / \mu_i m_H}$ is the sound speed of ionized gas at the electron temperature T_e , k_B is the Boltzmann constant, $\mu_i = 1.4$, m_H is the mass of the atomic hydrogen, and the factor of 2.2 appears owing to that there are 2.2 free particles per H nucleus (0.1 He per H, and 1.1 electrons per H, Krumholz 2017). The total external pressure can be expressed as below:

$$P_{\text{ex}} = P_{\text{IBL}} + P_{\text{ram}} = 2\rho_i c_i^2 = 2n_e m_H c_i^2. \quad (1)$$

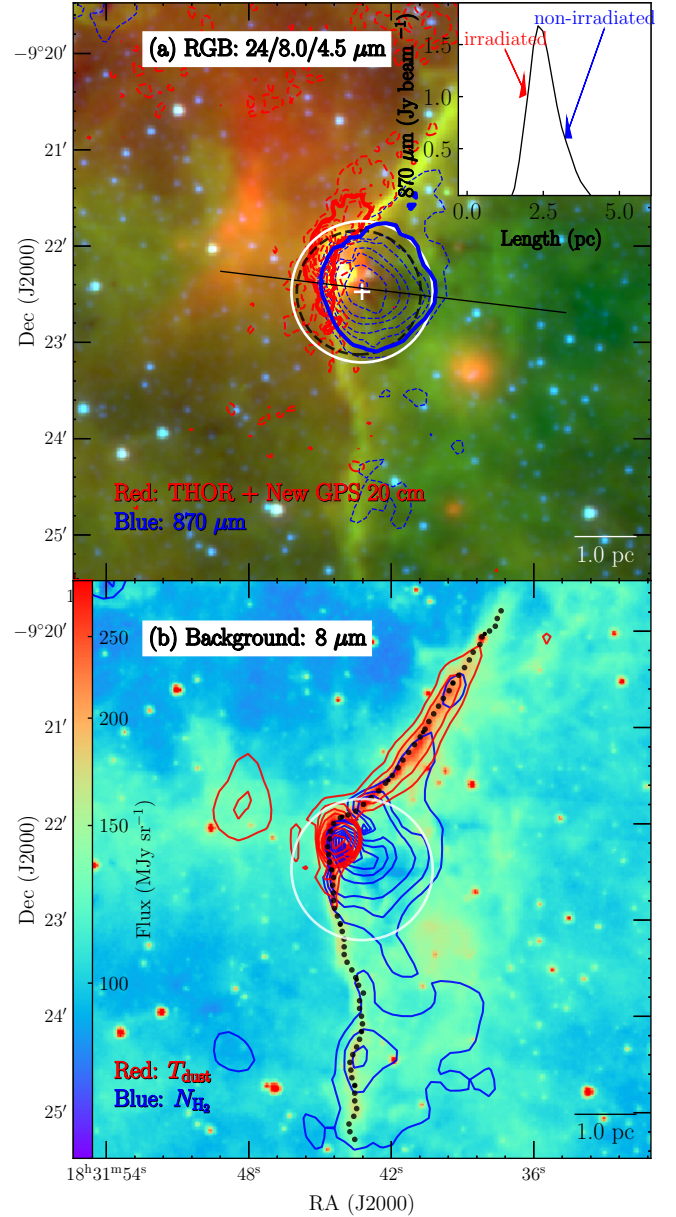


Figure 2. Environment of I18290. *Panel a:* *Spitzer* 24/8.0/4.5 μm RGB image overlaid with the contours of 20 cm (red dashed) and ATLASGAL 870 μm (blue) continuum. The levels of 20 cm continuum are [4, 5, 6, 7, 8, 9, 10, 12, 14, 16] $\times \sigma_{20 \text{ cm}}$, where noise of the 20 cm image $\sigma_{20 \text{ cm}} = 0.45 \text{ mJy beam}^{-1}$. The red bold contour of 20 cm emission (level: $2.38 \text{ mJy beam}^{-1} = 40\%$ of the continuum peak) highlights the region considered in the IBL calculations. The levels of 870 μm emission are [0.2, 0.3, 0.4, 0.5, 0.7, 0.9, 1.3, 1.8] Jy beam^{-1} . The white and black circles indicate the ATOMS-imaged field and the clump effective radius r_{clp} given by Urquhart et al. (2018), respectively. The blue bold contour of 870 μm continuum with a level of $0.3 \text{ mJy beam}^{-1}$ indicates a region with a size roughly equivalent to the circle size of r_{clp} . The *small panel* shows the 870 μm intensity profile along the black line. *Panel b:* The 8 μm emission overlaid with the contours of the *Herschel* dust temperature T_{dust} (red) and column density N_{H_2} (blue), with levels of [21.3, 21.6, 21.9, 22.2, 23.2, 24.2, 25.2] K and [2.4, 2.7, 3, 4, 5, 6, 7, 8, 9, 10] $\times 10^{22} \text{ cm}^{-2}$, respectively. The dotted line marks the rim spine extracted by Filfinder from 8 μm image.

Using an electron number density n_e of 240 cm^{-3} derived from the 20 cm free-free emission and an electron temperature T_e of 7180 K derived from the empirical relation between T_e and Galactic distance R_{GC} , we have $P_{\text{ex}}/k_B \approx 5.7 \times 10^6 \text{ K cm}^{-3}$. Here the details of calculating n_e and T_e can be found in Appendix C2.

We then estimate the clump inner pressure $P_{\text{in}} \approx \rho_{\text{in}} \sigma_{\text{1D}}^2$, where ρ_{in} and σ_{1D} are the clump mass density and the deconvolved 1D velocity dispersion, respectively. Considering that ^{13}CO traces intermediate-density gas compared to CO and C^{18}O , and that ^{13}CO higher transitions trace warmer and denser gas compared to $J = 1 - 0$ (e.g. $E_u = 5.5$ and 33.2 K for $J = 1 - 0$ and $J = 3 - 2$, respectively), we use FOREST Unbiased Galactic plane Imaging survey with the Nobeyama 45 m telescope (FUGIN, Umemoto et al. 2017) $^{13}\text{CO } J = 1 - 0$ to derive $\sigma_{\text{1D}}^2 = \sigma_{\text{sp}}^2 - \sigma_{\text{ch}}^2$. The σ_{ch} and σ_{sp} are the velocity dispersions for the channel and the fitted Gaussian of clump-averaged spectra, respectively. The corresponding spectra are presented in Appendix Fig. B2. The clump radius $r_{\text{clp}} \approx 1 \text{ pc}$ is from the effective radius given by Urquhart et al. (2018), which corresponds a size approximately equivalent to the region with the ATLASGAL $870 \mu\text{m}$ emission above $0.3 \text{ mJy beam}^{-1}$ (indicated by the blue bold contour in Panel a of Fig. 2). We have $P_{\text{in}}/k_B = 3.4 \pm 1.0 \times 10^6 \text{ K cm}^{-3}$ with $\sigma_{\text{sp}, ^{13}\text{CO } J=1-0} = 1.66 \text{ km s}^{-1}$.

The derived P_{ex} is in a range similar to those of the low-mass BRCs surveyed by Thompson et al. (2004b). In the most massive BRC that RDI has been discussed, BRC@CN20 ($M_{\text{clp}} \approx 5.2 \times 10^3 \text{ M}_{\odot}$), Ortega et al. (2016) derived $P_{\text{in}}/k_B = 1.2 \pm 0.5 \times 10^8 \text{ K cm}^{-3}$ and $P_{\text{ex}}/k_B = 5.4 \pm 2.5 \times 10^6 \text{ K cm}^{-3}$, illustrating that BRC@CN20 IBL compression is too weak compared to the clump inner pressure and therefore RDI is unable to operate.

Differing from BRC@CN20, I18290 has an over-pressure IBL compressing the clump. The virial status of I18290 can be significantly changed by this compression. First, we take into account two simplified cases for the external pressure, P_{ex} , from ionized gas: (1) *The IBL enshrouds the whole clump surface.* The corresponding virial equation without magnetic fields and rotation is expressed as (Lequeux 2005; Bodenheimer 2011):

$$F = 2U + \Omega - 4\pi r_{\text{clp}}^3 P_{\text{ex}}, \quad (2)$$

where the internal kinetic energy U and the potential energy Ω are

$$U = \frac{3}{2} M_{\text{clp}} \sigma_{\text{1D}}^2, \quad \Omega = -\frac{3}{5} \alpha \beta \frac{G M_{\text{clp}}^2}{r_{\text{clp}}}. \quad (3)$$

The factors α and β are related with power-law index of the density profile and clump eccentricity (Li et al. 2013), respectively. Using α derived from the $870 \mu\text{m}$ radial profile at the irradiated side and β derived from the $870 \mu\text{m}$ geometry (Urquhart et al. 2014), we find that $F < 0$ and there is no solution of the virial mass M_{vir} for the quadratic equation $F(M_{\text{vir}}) = 0$. Thus, I18290 is always bound or subvirialized. (2) *Without the external pressure from IBL.* This could be treated as the pre-compression status. With $P_{\text{ex}} = 0$ and α derived from the $870 \mu\text{m}$ emission radial profile at the non-irradiated side, we solve $F(M_{\text{vir}}) = 0$. The resulting $M_{\text{vir}} \approx 2320 \text{ M}_{\odot}$. Consequently, I18290 is unbound if IBL compression is ignored.

Second, the IBL actually only covers a part of the clump surface rather than the whole surface. The factor of 4π in the pressure item of Eq. 2 could be replaced by an actual solid angle θ covered by the IBL on the clump surface. The potential energy Ω is correlated with the distribution of density (α) and the shape of clump (β). The changes of IBL coverage θ propagates to α and β due to the corresponding changes of compression. Therefore, the full form of the $F - \theta$ equation is much complicated. A steeper density profile and a more elongated shape lead to a more bound status for clump (Li et al. 2013). Here

we simply estimate a critical IBL coverage solid angle θ_{cri} , which is the minimum solid angle allowing IBL to bind the clump. By setting $F(M_{\text{clp}}) = 2U + \Omega - \theta_{\text{cri}} r_{\text{clp}}^3 P_{\text{ex}} = 0$, α derived from non-irradiated sides and β derived from a spherical shape (to have a smaller $|\Omega|$), we have an upper limit of 3.5 rad for θ_{cri} . Accounting for this small θ_{cri} which is around a quarter of the clump surface, it is rational to suggest that the clump is still bound even considering the actual coverage of IBL.

Recalling our previous virial calculations without external pressure for the candidate high-mass starless clumps which are impacted or non-impacted by ionized regions (Zhang et al. 2020), we found a noteworthy difference that 90% of the non-impacted clumps are bound while only 50% of the impacted clumps are bound. The lower bound fraction for the impacted high-mass starless clumps could be just a biased result because the ignored IBL compression could contribute significantly in binding clumps.

4 SEQUENTIAL STAR FORMATION WITHIN CLUMP-FED SCENARIO

The observations targeting RDI in low-mass cases reveal that star formation follows a small-scale ($\lesssim 1 \text{ pc}$) age sequence along the direction of ionizing radiation. The more evolved protostars or cores are closer to the exciting massive stars. This sequential star formation is thought to be a relic of shock propagation. The shock driven by over-pressure IBL propagates into the clump's interior and then triggers clumps/cores to collapse and sequentially form stars (Sugitani et al. 1995; Fukuda et al. 2002; Ikeda et al. 2008; Getman et al. 2009; Chauhan et al. 2009; Choudhury et al. 2010; Fukuda et al. 2013; Panwar et al. 2014; Imai et al. 2017). Following the shock speed estimation formula and methods in Urquhart et al. (2007):

$$v_{\text{shock}}^2 = \alpha_{\text{shock}} \frac{(P_s - P_n)}{\rho_n}, \quad (4)$$

where P_s is the shocked gas pressure, and P_n and ρ_n are the pressure and mass density of the pre-shock gas, respectively. The α_{shock} is a factor about one to two, depending on the detailed properties of the shock (White et al. 1999). Assuming $P_s = P_{\text{ex}}$, $P_n = P_{\text{in}}$, and $\rho_n = \rho_{\text{in}}$, the estimated v_{shock} is about 1.5 km s^{-1} . Therefore, the squeezing exerted by I18290 IBL may power a shock with a velocity of $\sim 1.5 \text{ km s}^{-1}$ that triggers star formation sequentially via RDI. We should note that the uncertainties of shock speed estimation may be large and the estimated shock speed is meaningful only regarding the order of magnitude. To explore the star formation activities in I18290, we first extract candidate dense cores and YSOs and then compare their evolutionary stages.

4.1 Dense cores

The dust dense cores are extracted from the ATOMS 3 mm continuum image using Astrodendrogram (Rosolowsky et al. 2008). A total of five extracted cores (C1 to C5) with masses from 8 to 76 M_{\odot} are shown and listed in Fig. 3 and Table 1, respectively (see details of the Astrodendrogram extraction and physical properties estimation in Appendix E1). The contamination from free-free emission of the ionized gas on the 3 mm flux is minimal because of non detection of the VLA 20 cm & 6 cm continuum emission (VLA beam $\sim 5''$, sensitivity ≈ 0.2 to $0.4 \text{ mJy beam}^{-1}$, Helfand et al. 2006) and the ATOMS H40 α line emission for these cores.

Table 1. Physical parameters of cores.

Core	Associated YSO ^(a)	$T_{\text{kin}}^{(b)}$ K	Min $T_{\text{kin}}^{(b)}$ K	Max $T_{\text{kin}}^{(b)}$ K	$M_{\text{core}}^{(c)}$ M_{\odot}	$M_{\text{core}}^{\text{cold}(c)}$ M_{\odot}	$M_{\text{core}}^{\text{warm}(c)}$ M_{\odot}	r_{core} AU	Σ_{core} g cm ⁻²	N_{H_2} 10 ²³ cm ⁻²	n_{H_2} 10 ⁶ cm ⁻³
C1 ^(d)	YSO #9	21.0	6.3	27.3	102.3±38.9	458.4±174.4	76.8±29.2	4656±465	13.3±4.3	28.5±9.2	30.6±10.4
C2		17.7	17.2	17.9	36.1±14.3	37.1±14.7	35.5±14.1	4905±490	4.2±1.4	9.0±3.1	9.2±3.3
C3		22.0	18.4	23.4	24.0±9.1	29.4±11.2	22.4±8.5	3033±303	7.4±2.4	15.7±5.1	26.0±8.8
C4	YSO #10	26.7	24.5	28.7	12.0±4.7	13.1±5.2	11.1±4.4	3949±394	2.2±0.7	4.6±1.6	5.9±2.1
C5		18.8	17.1	22.4	8.2±3.1	9.2±3.5	6.8±2.6	1828±182	7.0±2.3	14.8±4.8	40.7±13.8

^(a) Candidate YSOs associated with 3-mm cores, see Table 2.

^(b) VLA beam-averaged NH₃ kinetic temperature T_{kin} , and the NH₃ max T_{kin} and min T_{kin} in the corresponding core's area, respectively.

^(c) M_{core} , $M_{\text{core}}^{\text{warm}}$, and $M_{\text{core}}^{\text{cold}}$ are the core masses with the beam-averaged T_{kin} , the max T_{kin} , and the min T_{kin} , respectively.

^(d) C1 is located on the edge where NH₃ intensity decreases dramatically due to effect from IBL. Therefore, the mass of C1 derived from the max pixel T_{kin} ($M_{\text{core}}^{\text{warm}}$) is probably more accurate than that derived from the beam-averaged T_{kin} (M_{core}).

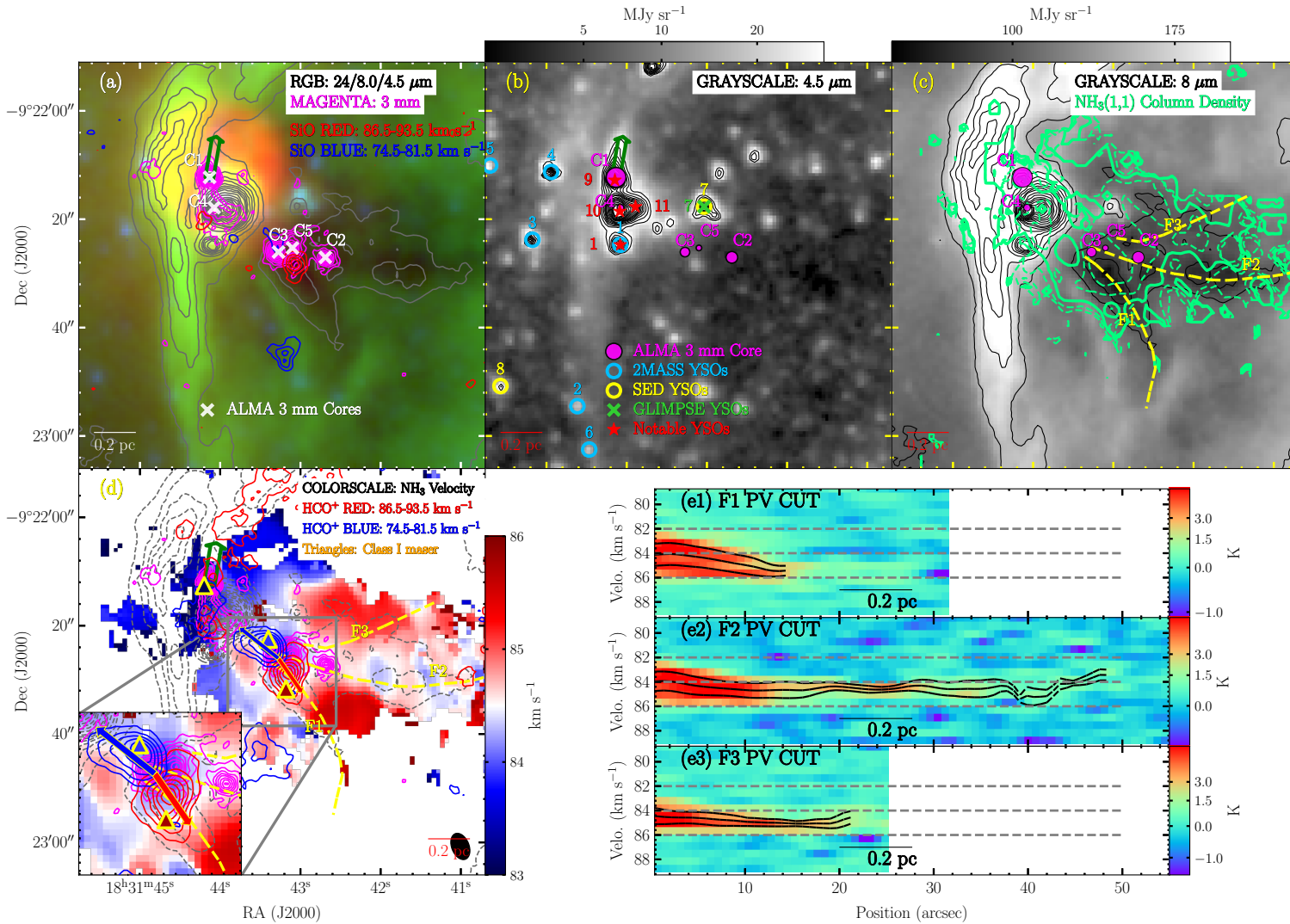


Figure 3. Star formation in the I18290 region. *Panel a:* *Spitzer* 24/8.0/4.5 μm RGB image overlaid with 8 μm emission (the gray contours: [0.8, 0.9, 1, 1.5, 2, 2.5, 3, 3.5, 4, 4.5, 5, 6, 7, 8, 9, 10, 11, 12, 13, 14] $\times 100 \text{ MJy sr}^{-1}$), SiO outflow lobes (the red and blue contours: [2, 3, 4, 5, 6, 7, 8, 9, 10] $\times \sigma_{\text{SiO lobe}}$, where image noise $\sigma_{\text{SiO lobe}} = 1.5 \text{ K km s}^{-1}$), and 3 mm continuum (the magenta contours: [3, 5, 7, 9, 11, 14, 17, 20, 23] $\times \sigma_{3 \text{ mm}}$, where noise of the 3 mm continuum image $\sigma_{3 \text{ mm}} = 0.08 \text{ mJy beam}^{-1}$). *Panel b:* Grayscale image and the black contours (levels: [3, 4, 5, 6, 7, 8, 9, 10, 12, 14, 16, 18, 20, 24, 28, 32] $\times 10 \text{ MJy sr}^{-1}$) show 4.5 μm emission, overlaid with 3-mm cores and extracted YSOs (see all YSOs in Table 2). The circles show the 3-mm cores with a size in proportion to core mass. The green arrow indicates EGO extended 4.5 μm emission. *Panel c:* Grayscale image and the black contours show 8 μm emission, overlaid with the light green contours of NH_3 column density N_{NH_3} derived from *fiteach* (levels: [14.5, 14.75, 15, 15.25, 15.5] $\times \log(10) \text{ cm}^{-2}$) with a highlighted level of 10^{15} cm^{-2} (solid contour). The yellow dashed lines outline filaments. *Panel d:* NH_3 centroid velocity derived from *fiteach*. The lobes of HCO^+ outflow are shown in the red and blue contours (levels: [2, 3.5, 5, 6.5, 8, 9.5, 11, 12.5] $\times \sigma_{\text{HCO}^+ \text{ lobe}}$, where the image noise $\sigma_{\text{HCO}^+ \text{ lobe}} = 2 \text{ K km s}^{-1}$). The red and blue arrows indicate outflow directions and lengths. The gray contours show the 8 μm emission. The triangles show CH_3OH Class I masers found by Rodríguez-Garza et al. (2017), with a color indicating maser velocity. The beam size for the observations of Rodríguez-Garza et al. (2017) is $\sim 2''$. The black ellipse shows the VLA beam of NH_3 image. *Panels e1, e2, and e3:* NH_3 (1,1) main line position-velocity cuts along filaments. The black lines mark the line centroid and dispersion fitted with *fiteach*.

The detected cores can be explained by a clump-to-core fragmentation dominated by thermal motions, under a mass sensitivity of $1.1 \text{ M}_\odot \text{ beam}^{-1}$ estimated from the rms level ($0.08 \text{ mJy beam}^{-1}$) of the continuum map assuming $T_{\text{dust}} = 20 \text{ K}$. With thermal Jeans fragmentation, the clump is expected to fragment to thermal Jeans cores with a mass and separation around M_J^{th} and λ_J^{th} :

$$M_J^{\text{th}} = \frac{4\pi\rho}{3} \left(\frac{\lambda_J^{\text{th}}}{2} \right)^3 = \frac{\pi^{5/2}}{6} \frac{\sigma_{\text{th}}^3}{\sqrt{G^3\rho}}, \quad \lambda_J^{\text{th}} = \sigma_{\text{th}} \left(\frac{\pi}{G\rho} \right)^{1/2}, \quad (5)$$

where σ_{th} is the thermal velocity dispersion

$$\sigma_{\text{th}} = \left(\frac{k_B T}{\mu m_H} \right)^{1/2}. \quad (6)$$

The mean molecular weight per free particle $\mu = 2.37$ because σ_{th} is governed by H_2 and He. When taking into account of both thermal and non-thermal motions, the corresponding turbulent Jeans parameters are

$$M_J^{\text{tot}} = \frac{\pi^{5/2}}{6} \frac{\sigma_{\text{tot}}^3}{\sqrt{G^3\rho}}, \quad \lambda_J^{\text{tot}} = \sigma_{\text{tot}} \left(\frac{\pi}{G\rho} \right)^{1/2}, \quad (7)$$

where the total velocity dispersion $\sigma_{\text{tot}} = (\sigma_{\text{th}}^2 + \sigma_{\text{nth},^{13}\text{CO}}^2)^{1/2}$, the $^{13}\text{CO } J = 1 - 0$ non-thermal dispersion $\sigma_{\text{nth},^{13}\text{CO}} = (\sigma_{\text{ID}}^2 - \sigma_{\text{th},^{13}\text{CO}}^2)^{1/2}$, and the $^{13}\text{CO } J = 1 - 0$ thermal dispersion $\sigma_{\text{th},^{13}\text{CO}} = (k_B T / \mu_{^{13}\text{CO}} m_H)^{1/2}$. The ^{13}CO molecule weight $\mu_{^{13}\text{CO}} = 29$. In the specific case that the compression of large scale supersonic flow creates density enhancement by a factor of Mach number squared M^2 , the Jeans parameters are (Zhang et al. 2021 and the references therein)

$$M_J^{\text{com,flow}} = \frac{\pi^{5/2}}{6} \frac{\sigma_{\text{nth},^{13}\text{CO}}^3}{\sqrt{G^3\rho_{\text{eff}}}}, \quad \lambda_J^{\text{com,flow}} = \sigma_{\text{nth},^{13}\text{CO}} \left(\frac{\pi}{G\rho_{\text{eff}}} \right)^{1/2}, \quad (8)$$

where effective density $\rho_{\text{eff}} = \rho M^2 = \rho (\sqrt{3} \sigma_{\text{nth},^{13}\text{CO}} / \sigma_{\text{th}})^2$.

We have $M_{J,\text{clp}}^{\text{th}} = 13 \pm 5 \text{ M}_\odot$, $\lambda_J^{\text{th}} = 0.46 \pm 0.1 \text{ pc}$; $M_{J,\text{clp}}^{\text{com,flow}} = 280 \pm 110 \text{ M}_\odot$, $\lambda_J^{\text{com,flow}} = 0.27 \pm 0.07 \text{ pc}$; and $M_{J,\text{clp}}^{\text{tot}} = 3020 \pm 1060 \text{ M}_\odot$, $\lambda_J^{\text{tot}} = 2.8 \pm 0.6 \text{ pc}$. These results suggest that other supportive mechanisms like turbulence and magnetic field only play marginal roles in I18290's fragmentation process. It is consistent with Liu et al. (2017b) and Zhang et al. (2021), who revealed a thermal fragmentation for the dense cores in massive clumps impacted by ionized regions, but different from the *Spitzer* mid-infrared observations of Sharma et al. (2016), which propose a non-thermally driven fragmentation for the YSOs embedded in BRCs.

4.2 Young stellar objects

Candidate YSOs (YSOs hereafter) are extracted from the GLIMPSE and 2MASS point source catalogs using color-color criteria or YSO SED models and then the background/foreground sources are excluded with the Gaia measurements (detailed extraction methods can be found in Appendix E2, Robitaille et al. 2006; Wang & Looney 2007; Gaia Collaboration et al. 2021). The YSOs with valid Gaia measurements are selected to keep those within the distance of [4.34, 6.34] kpc (1 kpc different from that of I18290) while the YSOs without Gaia measurements are simply assumed to have the same distance as I18290. With such selection, one of the two GLIMPSE, and six of

the nineteen 2MASS color-color selected YSOs, and two of the four SED fitted YSOs remain. The extended emission of the $8\text{-}\mu\text{m}$ rim PDR heavily influences source extraction and photometric measurements of the point sources. Therefore, three point sources bright at GLIMPSE band (YSOs #9, 10, 11 in Panel b of Fig. 3 and Table 2) are additionally included, which are located at the rim but not identified as YSOs by the three mentioned methods due to very bright background contamination in the IR images. All extracted YSOs are shown and listed in Panel b of Fig. 3 and Table 2, respectively.

There are a total of four sources are found at the rim, YSOs #1, 9, 10, and 11. YSOs #9 and 10 are associated with C1 and C4, respectively, whereas YSOs #1 and 11 are not associated with any detected core. YSO #11 is the brightest $8\text{-}\mu\text{m}$ point source and its $8\text{-}\mu\text{m}$ emission partly overlaps with the $8\text{-}\mu\text{m}$ emission of YSO #10 (C4). Gaia measurements suggest that YSO #11 is a foreground source located at a distance of $1.22^{+1.0}_{-0.38} \text{ kpc}$. YSO #1 seems to be a Herbig Ae/Be (HAeBe) star according to its 2MASS color (see Appendix E2). Whether YSO #1 is associated with I18290 is uncertain, no associated dense gas or dust emission is detected in the ATOMS data set. YSO #1 may couple with the rim structure based on the morphology that YSO #1 $8\text{-}\mu\text{m}$ emission is likely located in an emission dip in the zeroth moment maps of a number of the ATOMS molecules tracing the rim, such as CCH, CS, and SO shown in Appendix Fig. G1. This complementary morphology between the $8\text{-}\mu\text{m}$ emission of YSO #1 and the molecular emission of the rim can be explained as the dispersal of circumstellar dense gas by HAeBe star YSO #1, akin to the cases shown by Fuente et al. (1998, 2002).

4.3 Age sequence

The cores' kinetic temperature T_{kin} from NH_3 observations of Lu et al. (2014) follows a decreasing trend with the distance from the rim, from $\sim 27 \text{ K}$ for C1 and C4, then 20 K for C3 and C5, and finally 18 K for C2. The reason for this T_{kin} gradient is the combined heating from the external IBL and the internal protostars at various evolutionary stages. The cores and YSOs in I18290 could be divided into three groups according to their locations and evolutionary stages:

- *IR-bright protostellar sources closest to or on the top of the rim.* This group contains YSOs #9 (C1), 10 (C4), and possibly YSOs #1, 3, 4, and 5. The most massive core C1 is identified as an extended green object (EGO) whose $4.5\text{-}\mu\text{m}$ emission is proposed to be dominated by H_2 ($v = 0 - 0$, S(9, 10, 11)) from outflow shocked gas (Cyganowski et al. 2008; Rodríguez-Garza et al. 2017). The $4.5\text{-}\mu\text{m}$ emission of C1 shows an arc structure extending to north, and this $4.5\text{-}\mu\text{m}$ arc has a morphology parallel to and complementary to the $8\text{-}\mu\text{m}$ rim, which probably suggests that rim compression is reorienting C1 outflow (see green arrow in Panels a and b of Fig. 3). C1 is also powering the $\text{CH}_3\text{OH } 44 \text{ GHz}$ Class I (Rodríguez-Garza et al. 2017) and 6.7 GHz periodic Class II masers (Szymczak et al. 2015). Class I masers frequently correspond to outflow activities. The protostellar core C4 is probably powering very weak outflows traced by $\text{HCO}^+ J = 1 - 0$ line wings shown in Appendix Fig. F2. C4 is located on the extended arc which is bright at $4.5\text{-}\mu\text{m}$ and 3 mm and also roughly parallel to the $8\text{-}\mu\text{m}$ rim, indicating a strong rim compression similar to C1 again. IR-bright massive protostellar cores have a probable age of $\lesssim 0.3 \text{ Myr}$ according to Motte et al. (2018). The remaining YSOs are likely to be HAeBe (YSOs #1, 4) or Class II YSOs (YSOs #3, 5) according to their 2MASS colors (see Appendix E2). Their likely typical age is $\sim 1 \text{ Myr}$ (van Dishoeck & Blake 1998; Manoj et al. 2006).

- *IR-quiet protostellar sources more distant from the rim.*

Table 2. Candidate YSOs.

YSOs	RA °	DEC °	D ^(a) kpc	GLIMPSE	2MASS	J ^(b) mag	H mag	K _S mag	3.6 μ m mag	4.5 μ m mag	5.8 μ m mag	8.0 μ m mag	Method ^(c)
1	277.933667	-9.37353	5.34	G022.3534+00.0648	18314408-0922247	15.11	14.402 ± 0.129	12.636 ± 0.064	10.713 ± 0.163	9.983 ± 0.167	8.33 ± 0.085		2MASS
2	277.935895	-9.381802	5.34		18314461-0922544	17.339	16.078	13.892 ± 0.078					2MASS
3	277.93823	-9.373271	5.34	G022.3556+00.0610	18314517-0922237	16.248	13.384 ± 0.074	11.742 ± 0.044	10.546 ± 0.055	10.533 ± 0.083	10.291 ± 0.122		2MASS
4	277.937258	-9.369796	5.34	G022.3582+00.0634	18314494-0922112	17.164	14.434 ± 0.08	12.03 ± 0.031		10.045 ± 0.15	9.356 ± 0.268		2MASS
5	277.940428	-9.369465	5.34	G022.3600+00.0608	18314570-0922100	17.178	14.803	13.441 ± 0.062	12.129 ± 0.084	11.868 ± 0.134	11.683 ± 0.215		2MASS
6	277.935281	-9.384027	5.34	G022.3448+00.0586	18314446-0923024	14.32	14.268 ± 0.101	13.341 ± 0.054	12.522 ± 0.128	12.448 ± 0.135			2MASS
7	277.929311	-9.371574	5.34	G022.3531+00.0696	18314301-0922174	15.392 ± 0.265	13.053 ± 0.08	11.801 ± 0.04	10.34 ± 0.246	10.029 ± 0.118	9.2 ± 0.053	8.324 ± 0.15	GLIMPSE+SED
8	277.939892	-9.380771	5.34	G022.3498+00.0561	18314555-0922506	15.841 ± 0.102	13.352 ± 0.024	12.263 ± 0.024	11.461 ± 0.06	11.403 ± 0.075	11.243 ± 0.114	11.147 ± 0.158	SED
9	277.933946	-9.370218	5.34	G022.3564+00.0662						9.225 ± 0.162	8.267 ± 0.068		
10	277.933692	-9.371816	5.34	G022.3549+00.0656						8.202 ± 0.177	6.876 ± 0.122		
11	277.932878	-9.37158	1.22		18314389-0922176	14.069	13.939 ± 0.111	12.525 ± 0.087					

(a) If there is no Gaia measurement, an assumed distance of 5.34 kpc for candidate YSOs is used.

(b) Measurements without error are upper limit magnitudes.

(c) Labels “2MASS”, “GLIMPSE”, and “SED” mark the YSO extraction methods described in Appendix E2.

This group contains IR-quietest cores C3 and C5. The core C3 drives an outflow with a kinematic age of 18 kyr and an outflow mass rate \dot{M}_{out} of $2 M_{\odot} \text{ kyr}^{-1}$ (detailed outflow calculations can be found in Appendix D2). C5 is very close to C3 (~ 0.05 pc) and may also power an outflow lobe toward the south but it is hard to be distinguished from C3 outflow from channel maps. The probable age of C3 and C5 is $\lesssim 0.1$ Myr if we follow the age statistics of IR-quietest high-mass protostellar cores in *Motte et al. (2018)*.

- *Prestellar core candidate most distant from the rim.* No outflow is detected towards massive core C2 ($\sim 36 M_{\odot}$). The narrow line widths of the ATOMS spectra presented in Fig. 4 in addition to the non-detection of warm gas tracers in the ATOMS wide spectral windows (97.52-99.39 GHz and 99.46-101.33 GHz, see Appendix Fig. F4) also support the interpretation that C2 is a candidate high-mass prestellar core with a probable age of 0.01 to 0.07 Myr according to the statistics of *Motte et al. (2018)*.

On the whole, the three groups of cores/protostars reveal a bona fide age sequence along the direction of ionization flux: the most evolved protostars are closest to the rim PDR and the candidate high-mass prestellar core is the farthest from the rim PDR whereas the IR-quietest protostellar cores (possibly) powering outflows are located in between. This small-scale age sequence is another piece of evidence for the ongoing RDI process. However, we should note that the age sequence presented in a scale smaller than GMC can be erased by redistribution of the triggered and spontaneously formed stars during evolution of the feedback-driven structure (*Dale et al. 2015; González-Samaniego & Vazquez-Semadeni 2020*). Another potential bias is that the age sequence is observed on 2D sky plane and thus projection may influence our result. A deviation from the observed age sequence is seen for YSO #7 which is classified as a Class II YSO with an age of $0.49^{+2.01}_{-0.39}$ Myr and a mass of $1.1 M_{\odot}$ given by YSO SED fitting. C2, C3, and C5 are exactly at the converging end of three filamentary arms (see the next section) whereas YSO #7 is offset from this convergent end, which is probably a hint that YSO #7 is a spontaneously formed star or redistributed star, or just a background/foreground star.

4.4 Feeding cores via filaments

The $8 \mu\text{m}$ extinction presented in Fig. 3 displays a morphology of several filamentary dark lanes converging to the IR-quietest cores C2, C3, and C5. Visually, we outline tracks of the maximum $8 \mu\text{m}$ extinction for the three most significant filamentary arms F1, F2, and F3 in Panel c of Fig. 3. The convergent morphology indicates that the gas is probably inflowing along filaments onto cores (*Ren et al. 2021*). The zeroth moment maps presented in Appendix Fig. G1 of several molecular line emission (i.e. HCO^+ , HCN, SO, and CS)

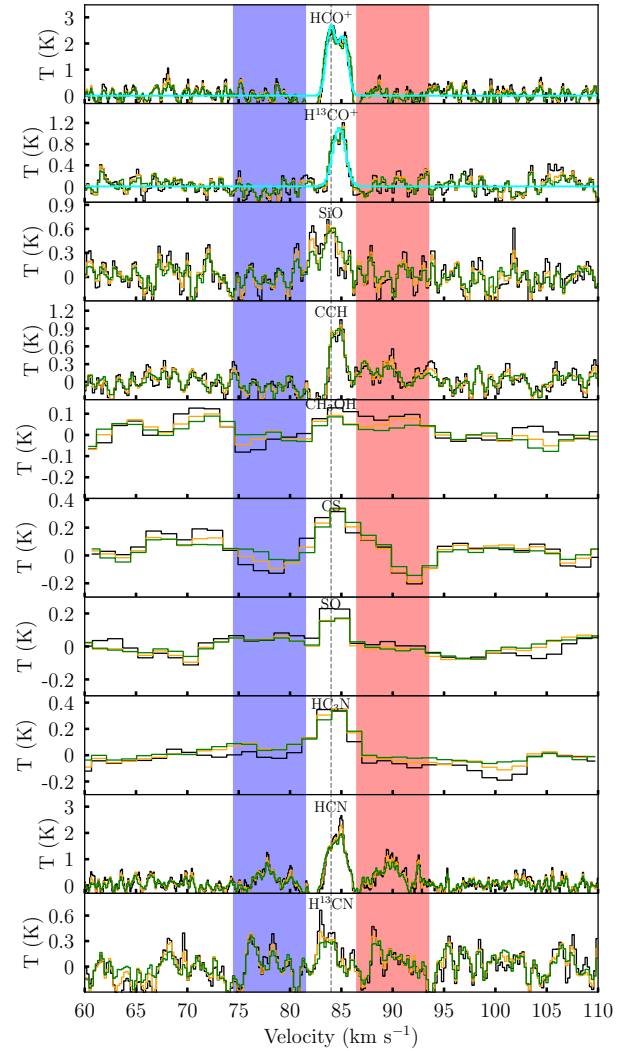


Figure 4. C2 ATOMS spectra. The spectra extracted from semi-axis, double semi-axes, and triple semi-axes areas are shown in black, orange, and green, respectively. The red and blue shadows indicate the velocity ranges of red and blue wings, respectively. The presented molecules include: HCO^+ , H^{13}CO^+ , HCN, H^{13}CN , SiO, CS, CCH, CH_3OH , SO, and HC_3N . Corresponding transitions could be found in Table 3 (only $N_{J,F} = 1_{3/2,2} - 0_{1/2,1}$ is shown for CCH). The gray dashed line shows the clump systemic velocity of 84 km s^{-1} . The $\text{H}115$ infall and Gaussian fitting results are shown with cyan lines in panels of HCO^+ and H^{13}CO^+ , respectively. The spectra of other cores can be found in Fig. 5 and Appendix F1.

observed with ATOMS do not show this filamentary morphology. To probe the gas kinematics, we make use of the VLA NH_3 data from Lu et al. (2014) which has the spatial and velocity resolutions of $\sim 4''$ (~ 0.1 pc) and 0.6 km s^{-1} , respectively. With the PySpecKit¹ task fiteach (Ginsburg & Mirocha 2011), we fit the NH_3 (1, 1) inversion lines to estimate NH_3 column density N_{NH_3} and centroid velocity. The NH_3 velocity map presented in Panel d of Fig. 3 shows that C3, C5, and possibly C2 are immersed in a blue-shifted “basin” with the red-shifted surroundings. It favors a possible scenario where the gas is infalling onto the group of IR-quiet cores (Estalella et al. 2019; Sepúlveda et al. 2020). The convergent filaments may represent the mainstreams of inflowing mass and hence play a critical role in transporting gas to the blue-shifted “basin”.

In Panels e1 to e3 of Fig. 3, we present the position-velocity (PV) cuts with a width of $5''$ (0.13 pc) along the filaments for NH_3 (1, 1) main line. A velocity change of 1 to 2 km s^{-1} is observed when moving to the inner ~ 0.4 -pc region surrounding the convergent center (velocity gradient $\approx 1.5 \text{ km s}^{-1}/0.4 \text{ pc}^{-1}$), in accordance with the blue-shifted “basin”. This velocity gradient is underestimated because of projection effect. The NH_3 observations can not resolve the filament width seen in the $8 \mu\text{m}$ image. To estimate the mass inflow rate along filament \dot{M}_{inflow} , we assume that the filaments have a width of 0.1 pc (estimated from $8 \mu\text{m}$ image), a NH_3 column density N_{NH_3} of 10^{15} cm^{-2} (shown in solid contour in Panel c of Fig. 3), and a $[\text{NH}_3/\text{H}_2]$ abundance of 3×10^{-8} (Lu et al. 2014), respectively. The estimated filament mass inflow rate $\dot{M}_{\text{inflow}} \sim M_{\text{fil}} \Delta v \tan(\alpha_p)^{-1}$ (Kirk et al. 2013), here $M_{\text{fil}} \sim 30 M_\odot$, Δv , and α_p are the filament mass, velocity gradient, and inclination to the plane of sky, respectively. Assuming $\alpha_p \sim 20^\circ$, the total resulted \dot{M}_{inflow} of three filaments is of the order of $1 M_\odot \text{ kyr}^{-1}$.

Another interesting observed morphology which possibly relates to filament inflow is that in the core C3, the $\text{HCO}^+ J = 1 - 0$ outflow red lobe has an edge similar to the NH_3 blue-shifted “basin”, shown as the zoom-in C3 region in Panel d of Fig. 3. Moreover, a Class I CH_3OH maser is also located on this edge. Given the hypothesis that collisional excitation pumping mechanism of Class I maser makes it able to trace the interface between outflow and surrounding materials (Cyganowski et al. 2009; Voronkov et al. 2014; Gómez-Ruiz et al. 2016), the Class I maser here may probe the gas shocked by the encounter of the C3 outflow and the inflowing filament material, similar to the case of SDC335 clump where the Class I masers are explained to be powered by the outflow-filament encounter (Avison et al. 2021).

To further address the inflow nature in the blue-shifted “basin”, we check the $J = 1 - 0$ spectral profiles of HCO^+ and H^{13}CO^+ for C2, C3, and C5 in Figs. 4, 5, and Appendix Fig. F3, respectively. The cores C3, C5, and possibly C2 present the blue asymmetries which indicate an inflow motion if T_{ex} decreases with the distance from core center (Zhou et al. 1993). Making use of the Hi115 infall model (De Vries & Myers 2005), we derive core-scale infall velocity v_{infall} from H^{13}CO^+ spectra (details of the Hi115 model and fitting procedure are in Appendix F). In the case that a blue asymmetry of H^{13}CO^+ profile is detected, HCO^+ spectra are not preferential because outflow components in HCO^+ profile can heavily bias the model fitting, such as the Hi115 modelling for HCO^+ spectra of C3 shown in Fig. 5. Core C2 v_{infall} is derived from HCO^+ because both self-absorption feature of H^{13}CO^+ profile and line wing of HCO^+ are weak. Note that we may overestimate the v_{infall} of C2 because the double-peak feature of HCO^+ profile is not conspicuous. The modelled v_{infall} are

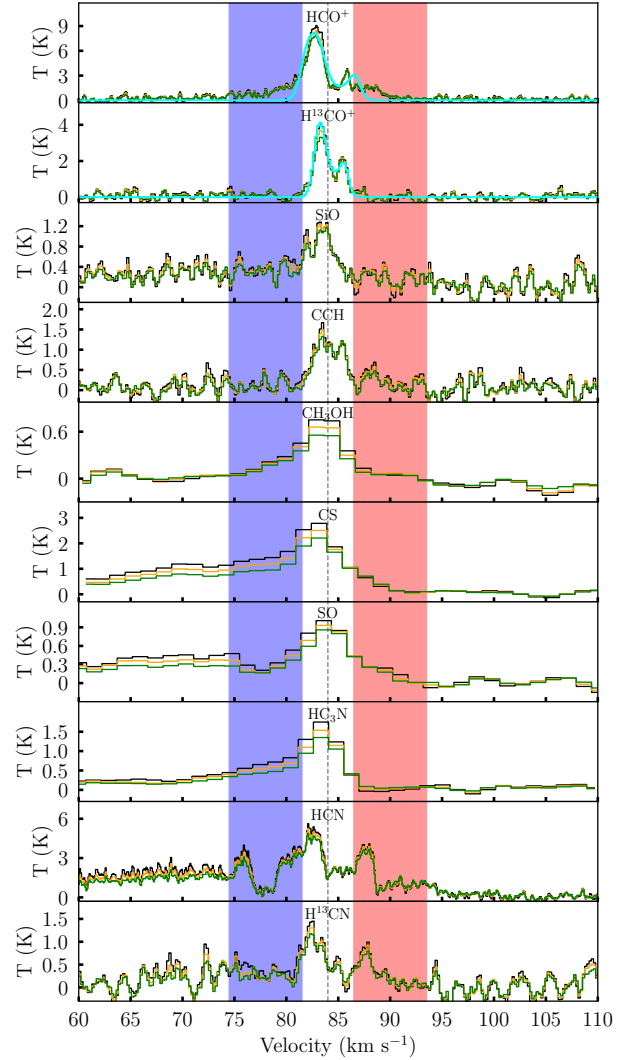


Figure 5. C3 ATOMS spectra. Similar to Fig. 4 except for that cyan lines in panels of HCO^+ and H^{13}CO^+ both show the Hi115 infall fitting results.

about 0.6, 0.5, and 0.1 km s^{-1} for C2, C3, and C5, respectively. The core-scale mass infall rates estimated via $\dot{M}_{\text{infall}} = 4\pi r^2 \rho v_{\text{infall}}$ (Contreras et al. 2018) are about 2.7, 2.6, and $0.23 M_\odot \text{ kyr}^{-1}$ for C2, C3, and C5, respectively. The derived core-scale infall rates are comparable to some similar observations toward HMSF regions, e.g. $3.5 M_\odot \text{ kyr}^{-1}$ within the innermost 500 AU for Beuther et al. (2013) and $1.9 M_\odot \text{ kyr}^{-1}$ within the innermost 8000 AU for Contreras et al. (2018).

Although the uncertainties in inclinations, molecule abundances, and calculation methods might be large, the filament inflow rate \dot{M}_{inflow} , core-scale infall rate \dot{M}_{infall} , and outflow rate \dot{M}_{out} are on the same order of magnitude, which sheds light on a continuous mass-building process from clump to core in I18290 BRC. IR-quiet massive cores C2, C3, C5 probably gain mass via filamentary arms embedded in the compression-subvirialized BRC, accompanied by ongoing sequential star formation, suggesting that a combined process of clump-fed accretion and RDI is functioning for HMSF in this BRC.

¹ <https://pyspeckit.readthedocs.io/en/latest/index.html>

5 DYNAMICAL PDR WITH PHOTOEVAPORATIVE FLOW

In this section, we further investigate structures and kinematics of the PDR traced by the 8- μm rim. CCH is one of the best tracers for the PDR in ATOMS data of I18290. Figure 6 shows that CCH $N_{J,F} = 1_{3/2,2} - 0_{1/2,1}$ (the strongest CCH hyperfine line in the ATOMS spectral window) zeroth moment has a spatial distribution analogous to the 8 μm emission. Pety et al. (2005) proposed that this correlation stems from the fact that PAHs can be the precursors of small hydrocarbons in the PDR. The formation and destruction mechanisms of CCH closely correspond to the energetic photons (Huggins et al. 1984; Teyssier et al. 2004; Cuadrado et al. 2015; Nagy et al. 2015; Buslaeva et al. 2021; Kirsanova et al. 2021), making CCH to be a great tracer of PDRs. We first compare the spatial distributions of CCH with other molecules and then analyze the rim PDR kinematics with CCH.

5.1 Associations of molecules and PDR

In addition to CCH emission, the PDR identified in the 8 μm image is also traced by several other molecular line emission from the ATOMS observations. Their zeroth moment maps are presented in Appendix Fig. G1 where some have poor signal-to-noise (SN) ratio. Using the method of structural similarity index measure (SSIM, Wang et al. 2004) which could compare the similarity of two maps, we categorize the molecules in Table 3 into two types according to their spatial similarity to CCH emission (details about SSIM and its calculations are in Appendix G1): (1) PDR tracers whose spectral zeroth moment maps have a morphology similar to CCH. The molecule most similar to CCH is H^{13}CO^+ , and then CS, HCO^+ , followed by SO and HCN. (2) star formation tracers, which only trace the gas directly related with star formation activities such as core dense gas and outflow. They include SiO, HC_3N , CH_3OH , and H^{13}CN . Note that our classifications of the PDR and star formation tracers are only valid for the ATOMS data of this region. Different data sets and star formation regions may lead to different members for these two groups.

PDRs represent transition regions from H II-dominated to H_2 -dominated with increasing A_V . The changes of UV radiation, H_2 density, and temperature create physical and chemical stratification from the exterior to the interior of PDRs, leading to a stratified distribution for the emission of various molecular species. Panel d of Fig. 6 shows the zeroth moment profiles of various PDR tracers along three cuts perpendicular to the rim PDR indicated in Panel a of Fig. 6. No consistent stratification is found in the three cuts and the zeroth moment profiles of various molecular species are peaked at the roughly same position.

This indistinctive stratification is probably caused by several reasons: (1) The resolution of 0.05 pc along with the noisy nature may be not enough to resolve the PDR stratification. In efforts to resolve the famous Orion Bar PDR, Goicoechea et al. (2016) find that the separation between ionization front and dissociation front is only ~ 0.03 pc, indicating that molecular stratification exists in a narrow space. Sicilia-Aguilar et al. (2019) searched for the stratification in BRC 1396A with a spatial resolution of 0.05 pc for a series of molecules, such as HCN, HCO^+ , CS, and SO but these authors find that the differences in peaks' position are only one to two beams. (2) The projection effects weaken the observed stratification feature when there is an inclination to the sky plane. (3) The vigorous gas flows in PDRs such as photoevaporative flow (PeF) and rocket effects may mix up the layered distributions. The PeF is off the clump surface and it is driven by the overpressure of the ionization/dissociation

Table 3. Molecular transitions in Sect. 5.

Molecular transition	Freq. GHz	SSIM peak ^(a)	Type ^(b)
CCH $N_{J,F} = 1_{3/2,2} - 0_{1/2,1}$	87.3169	-	PDR
CCH $N_{J,F} = 1_{3/2,1} - 0_{1/2,0}$	87.3286	0.359	PDR
$\text{H}^{13}\text{CO}^+ J = 1 - 0$	86.7543	0.256	PDR
CS $J = 2 - 1$	97.9810	0.245	PDR
$\text{HCO}^+ J = 1 - 0$	89.1885	0.229	PDR
SO $v = 0, 3(2) - 2(1)$	99.2999	0.218	PDR
$\text{H}40\alpha$	99.0230	0.191	SF
SiO $J = 2 - 1$	86.8470	0.188	SF
$\text{HC}_3\text{N } J = 11 - 10$	100.0764	0.185	SF
$\text{CH}_3\text{OH } 2(1,1) - 1(1,0)\text{A}$	97.5828	0.176	SF
VLA $\text{NH}_3 (1,1)$	23.6945	-	SF ^(c)
HCN $J = 1 - 0$	88.6318	-	PDR ^(d)
$\text{H}^{13}\text{CN } J = 1 - 0$	86.3399	-	SF ^(d)

^(a) Peak value of the channel-by-channel SSIM calculation figures presented in Appendix Fig. G2. A higher peak value indicates a higher similarity between spatial distributions of two molecular emission.

^(b) “PDR” and “SF” represent the PDR and star formation tracers, respectively.

^(c) VLA $\text{NH}_3 (1,1)$ is not included in the SSIM calculations because it is not observed by ALMA. No emission is associated with the 8- μm rim PDR in the zeroth moment map and thus NH_3 is simply set as SF tracer.

^(d) $J = 1 - 0$ of HCN and H^{13}CN are not included in the channel-by-channel SSIM calculations because their hyperfine emission could contaminate each other and then influences channel-by-channel SSIM calculations. A layer aligned with the 8- μm rim is presented in the zeroth moment map of HCN $J = 1 - 0$ but not for $\text{H}^{13}\text{CN } J = 1 - 0$ and therefore HCN and H^{13}CN are classified as PDR and SF tracers, respectively.

region compared to the cold molecular region. Moreover, the conservation of momentum impels the clump to move in the opposite direction. In the next section, we investigate the signatures of PeF in I18290.

5.2 Photoevaporative flow traced by CCH?

Many simulations in BRC clearly present the PeF with a velocity of around 1 to 10 km s^{-1} and a direction perpendicular to clump surface (Lefloch & Lazareff 1994; Kessel-Deynet & Burkert 2003; Miao et al. 2006, 2009; Haworth et al. 2013; Nakatani & Yoshida 2019). Observationally, however, the velocity fields show the explicit evidence of PeF only in a few BRCs. McLeod et al. (2015) analyzed S II spectra PV cut along the direction of ionization radiation for M16 (pillars of creation) and these authors find a blue-shifted dip of $\sim 10 \text{ km s}^{-1}$ in the PDR which is proposed to be a kinematic feature of PeF. In the PDR of BRC 1396A, Sicilia-Aguilar et al. (2019) find a remarkable second component besides the main component tracing the clump body (shift is $\sim 2 \text{ km s}^{-1}$) in CN spectra. These authors suggest that the second component is probably from PeF.

Here, we search for PeF with the CCH spectra. The core spectra presented in Figs. 4, 5, and Appendix Figs. F1 to F3 indicate that the CCH emission is relatively unrelated with core outflow motions in our case and therefore the contamination from star formation activities is weak. The CCH $N_{J,F} = 1_{3/2,2} - 0_{1/2,1}$ PV cuts along and perpendicular to the PDR spine (Panels b and c of Fig. 6) show a complicated velocity mode. For the three cuts perpendicular to the PDR spine, it is obvious that the CCH presents at least two velocity components around the spine (offset $\sim 0''$), whereas they merge to one component when moving to the clump interior (offset $> 0''$). The

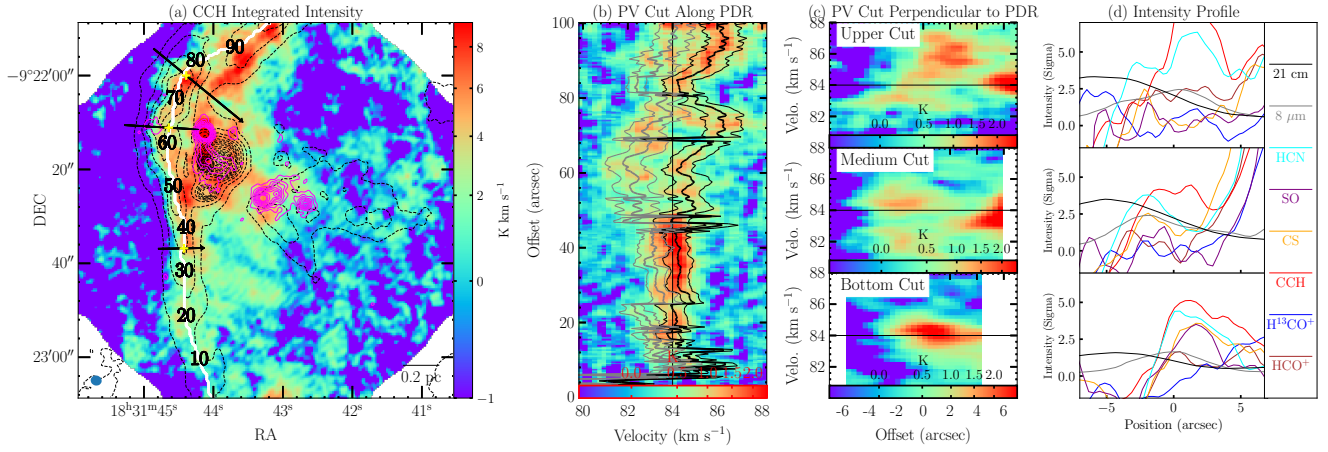


Figure 6. CCH $N_{J,F} = 13/2,2 - 01/2,1$ emission. *Panel a:* CCH integrated intensity maps overlaid with the contours of $8\ \mu\text{m}$ emission (black) and the 3 mm continuum (magenta) with levels the same as *Panel a* of Fig. 3. The white line indicates the $8\text{-}\mu\text{m}$ rim spine extracted by Filfinder in Sect. 3. The numbers on the spine indicate the offset positions corresponding to *Panel b*. *Panel b:* PV cut along the rim spine. The three black and gray lines show the MCMC-fitted compressed and PeF components with velocity centroid and dispersion, respectively. *Panel c:* PV cut (width = $5''$) along the three arrows shown in *Panel a*. *Panel d:* Intensity profiles of various species along the arrows. In *Panels c* and *d*, the zero offset positions are positions at the spine and a positive offset means a position close to the interior of the clump.

two-velocity structure is not due to self-absorption because stronger CCH lines in the region do not show a clear absorption feature.

To check the velocity feature in the entire observed PDR, a CCH PV cut with a width of $5''$ (to minimize the contamination associated with cores) is created along the PDR spine and shown in *Panel b* of Fig. 6. The southern parts seem to present a single velocity component with a blue wing. For the strongly irradiated BRC head ($40''$ to $80''$ position in *Panel b* of Fig. 6), the CCH emission splits into at least two well-separated components and becomes weaker compared to the southern parts. With a simplified assumption that the CCH PV cut along the PDR spine is composed of two Gaussian components at each position, we fit the PV cut position-by-position using the Markov Chain Monte Carlo (MCMC) method (fitting details are in Appendix G2). The spine PV cut is well modelled by two Gaussian components with the velocity dispersion of $\sim 0.5\ \text{km s}^{-1}$, and the velocity shifts of $\sim 1\ \text{km s}^{-1}$ for the southern part and 2 to $3\ \text{km s}^{-1}$ for the head. The fitting residual $\sim 0.17\ \text{K}$ is close to the noise of the CCH data cube.

We propose that these two velocity components are from PeF (blue-shifted) and compressed shell (red-shifted), respectively, based on the following observed features in the PV cut along the PDR spine:

- The red-shifted component is stronger than the blue-shifted component in the modelled CCH PV cut, which may stem from the fact that the compressed gas is denser than the PeF gas.
- The velocity shift between PeF and compressed components becomes larger at the BRC head, compared to that of the southern part. It is probably driven by more intense ionizing radiation in the BRC head than in the southern part, which powers a stronger compression and photoevaporation in the head to create a larger velocity shift. This enlargement of the velocity shift is also presented in some RDI simulations (Lefloch & Lazareff 1994; Miao et al. 2009; Haworth et al. 2013).
- CCH emission is weaker in the BRC head compared to the southern parts, which can be explained as a result of more intense photodestruction of CCH in the head.

All these observed signatures support the interpretation that the blue- and red-shifted components trace the PeF and compressed gas,

respectively. The ATOMS spectral window covers CCH hyperfine lines $N_{J,F} = 13/2,2 - 01/2,1$ and $N_{J,F} = 13/2,1 - 01/2,0$ which could in principle be used to derive CCH optical depths and T_{ex} under LTE conditions using hyperfine fitting tools (such as HFS tools in CLASS, Kirsanova et al. 2021). However, the CCH hyperfine line intensity ratio in I18290 PDR is very close to the theoretical value of optically thin emission in LTE, 2:1 ratio. Furthermore, the deviations from the single-Gaussian profile in most pixels and the low SN ratio of the weaker CCH $N_{J,F} = 13/2,1 - 01/2,0$ spectra cause large errors in the hyperfine fitting. Here we only estimate CCH column density N_{CCH} from the Gaussian components extracted by MCMC with the assumption of optically thin emission under LTE. The median N_{CCH} is about 10^{14} to $10^{15}\ \text{cm}^{-2}$ at a typical T_{ex} of 100 K, with the N_{CCH} ratios of compressed-to-PeF components of 1.1 for the southern parts and 2.7 for the head (see calculations in Appendix D3). The abundance of CCH in the PDR is highly variable and depends on the detailed physical and chemical status of the PDR, which is beyond the scope of this paper. Further assuming a CCH abundance of 10^{-8} (Teyssier et al. 2004; Nagy et al. 2015; Cuadrado et al. 2015; Buslaeva et al. 2021; Kirsanova et al. 2021), the column density of the PDR is of the order of 10^{22} to $10^{23}\ \text{cm}^{-2}$.

6 DISCUSSIONS AND CONCLUSIONS

The essence of the clump-fed scenario is the central role of inflow motions beyond core scale on mass building of HMSF. Detailed interferometric case studies, e.g. SDC335 (Peretto et al. 2013), G22 (Yuan et al. 2018), and G34 (Liu et al. 2022a), provide strong evidence for the pc-scale inflow. Peretto et al. (2020) proposed that the clump-fed rather than core-fed process is prevalent for the cores hosted in HMSF regions because the mass versus temperature evolutionary track resulted from the clump-fed scenario agrees better with their observations of ~ 200 cores in 11 massive IRDCs. Most of the studied clump-fed processes are working within pc-scale clumps with a quiescent environment. The necessity of merging external ionizing impact into clump-fed accretion scenarios comes from the prevalence of H II region in HMSF regions (Thompson et al. 2012; Zhang et al.

2021). Mainly existing works involving both ionizing feedback and accretion via filaments are the cases where H II regions in the central hub/ridge of hub-filament system (HFS) impact the density structure of the HFS and star formation therein (e.g., example observations by Baug et al. 2018; Watkins et al. 2019; Kumar et al. 2020; Dewangan et al. 2020; Liu et al. 2021b; modellings: González-Samaniego & Vazquez-Semadeni 2020; Whitworth & Priestley 2021). The studied interplay between accretion and ionizing feedback in these works has scales much greater than clumps (~ 1 pc).

The HMSF ongoing in BRCs is not brand new in observations considering that various tracers of HMSF embedded in BRCs have been found, such as UCH II regions (Morgan et al. 2004; Thompson et al. 2004b; Urquhart et al. 2004, 2006), masers (Valdettaro et al. 2005, 2007, 2008; Urquhart et al. 2009), and massive YSOs (Sharma et al. 2016), but a clear case of the filament-mediated accretion within clump accompanied with the signatures of triggered HMSF is not presented by previous observations of the clump-scale BRCs. The filament-mediated accretions within RDI-driven objects indeed exhibit in some simulations. Dale et al. (2014, 2015) proposed that pillars and globules are the relics of the filaments and accretion flows shaped by ionizing radiations whereas Bisbas et al. (2011) found that a filament aligned to the axis of symmetry can form due to the convergence of collapsing material during the evolution of BRC.

Our observations of I18290 BRC offer a pilot picture depicting a scene combined by the clump-fed and the ionizing feedback processes: The pressure exerted by photoionized clump surface constrains I18290 in a subvirial, bound state. Meanwhile, the shock driven by the overpressure of ionized surface propagates into the clump interior, and triggers a sequential star formation with a time scale of 0.1 to 1 Myr and a size scale of $\lesssim 1$ pc along the radiation direction. The resulted star formation propagation speed of 1–10 km s⁻¹ is not only on the same order as our estimated shock speed 1.5 km s⁻¹, but also similar to the shock speeds in the low-mass BRC observations and simulations (Marshall & Kerton 2019). These proofs support that induced star formation by RDI is at work in I18290. Compared to the RDI in low-mass case, a remarkable difference for massive I18290 BRC is the inflowing multi-filamentary arms developed in the clump during the RDI process. The filament inflows ($\sim 1 M_{\odot} \text{ kyr}^{-1}$) toward the massive core group, along with the strong core-scale infall ($\sim 2 M_{\odot} \text{ kyr}^{-1}$), imply that massive cores are gaining their mass from clump-wide environment.

The entire picture is very similar to the model of Anathpindika & Bhatt (2012) (A&B2012 hereafter) which is one of the most massive RDI simulations regarding a single BRC. Figure 7 shows a comparison between the schematic of I18290 and the clump modelled by A&B2012 at a snapshot time of 0.23 Myr. The model initial conditions are quite similar to the current conditions of I18290 estimated in our work, in respects of the clump size (~ 1 pc), density ($\sim 10^4 \text{ cm}^{-3}$), and turbulence (Mach number ~ 10). The similar physical conditions make sense to compare between the models and observations. I18290 presents a morphology strikingly similar to the model. The color-codings of various structures (cores, filaments, PDR shell, and clump) in the schematic of I18290 share the same colorbar of the model panel. Although the observed densities of extended structures (shell and filaments) are one magnitude smaller than in the model owing to beam dilution, a density amplification of one to two orders of magnitude compared to the clump density for these extended structures is akin. I18290 reproduces two main sites of star formation in the model: the dense PDR shell and the central core group with inflowing extended filamentary arms. The modelled averaged star formation rate (SFR) $\sim 0.1 M_{\odot} \text{ kyr}^{-1}$ is likely of the

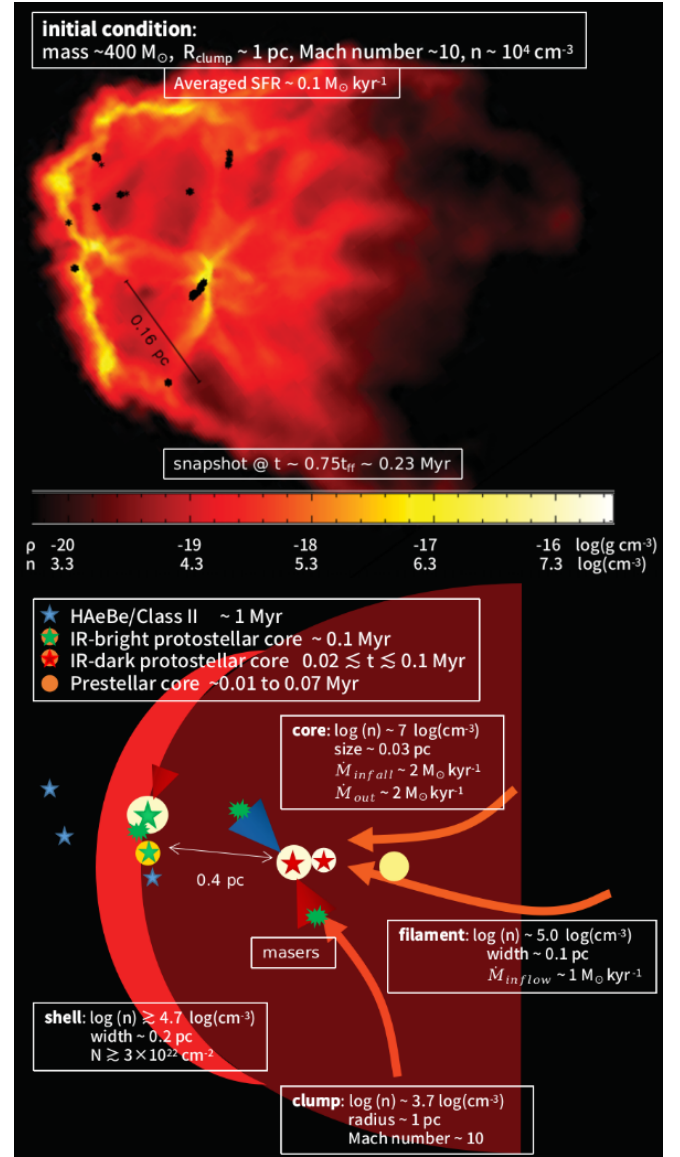


Figure 7. Comparison with model. *Top panel:* Density map of the simulated massive BRC, adapted from Anathpindika & Bhatt (2012) with permission. Sink particles are indicated with black asterisks “*”. *Bottom panel:* Schematic of I18290. The color-coding of various structures (clump, shell, filament, and cores) follows the same colorbar as *top panel*.

same order as in I18290 if we assume a timescale of ~ 0.5 Myr and a total stellar mass of $\sim 50 M_{\odot}$ for I18290.

There are still some notable differences between I18290 and the model: (1) The cores and YSOs identified in I18290 are significantly less than the modelled sink particles that represent forming stars, which could stem from the poor mass sensitivity of the ATOMS data ($1.1 M_{\odot} \text{ beam}^{-1}$). (2) The corrugated and broken nature of the PDR shell driven by thin-shell instabilities for the model is ambiguous for the observed PDR shell. The possible reason is that the limited resolution and sensitivity dilute the fluctuations at a smaller scale. (3) Sink particles in the modelled shell seem to spread over a larger fraction of shell compared to the cores and YSOs in the shell of I18290. Unfortunately, whether this difference is real is unknown

because A&B2012 did not present the detailed properties of the individual sink particles such as age and mass.

It will be very interesting to model how the external feedback influences star formation in a scale comparable to or smaller than cores in future work. Outflows near the rim PDR such as C1 outflow may be reoriented due to the compression of ionized surface. Furthermore, the $\text{HCO}^+ J = 1 - 0$ spectra for the cores (C1 and C4) close to the rim present a red asymmetry indicating expansion. A more striking phenomenon is that the core C1 Class II CH_3OH masers within a scale of $0.1''$ (500 AU) seem to align with the large-scale PDR shell (see distribution of Class II masers with a velocity $> 81 \text{ km s}^{-1}$ in Figure 9 of Szymczak et al. 2015). Dodson et al. (2004) proposed that the linear distribution of Class II masers could be caused by an edge-on planar shock propagating into a star-forming core. This scenario may cast light on the potential strong effect of IBL on the interior of core C1.

The outflows sustain a large fraction of I18290 turbulence because the outflow energy rate \dot{E}_{out} is of the same order as the turbulent dissipation rate for I18290 (Baug et al. 2021). The gas kinematics are not presented in the A&B2012 model. It is worthwhile to model and analyze the various gas flows that exist in the irradiated turbulent massive BRC, such as photoevaporation flow and filament inflow (Haworth et al. 2013), especially for the questions whether a bound clump status under the assistance of IBL could significantly increase accretion rate of cores in massive clumps (Motoyama et al. 2007; Maheswar & Bhatt 2008).

This pilot observational study investigates the triggered star formation via RDI within clump-fed scenario for a massive BRC. Forthcoming ALMAGAL data which involves a few dozens of massive BRCs shown in Fig. 1 will help us construct a more complete picture, especially for the universality of this combined mechanism in massive BRCs.

ACKNOWLEDGEMENTS

We want to thank the anonymous referee for the constructive comments that helped improve a lot quality of the paper. S.Z. and K.W. acknowledge support from the China Manned Space Project (CMS-CSST-2021-B06, CMS-CSST-2021-A09), the National Science Foundation of China (11973013, 12033005), the National Key Research and Development Program of China (2019YFA0405100), and the High-performance Computing Platform of Peking University through the instrumental analysis fund of Peking University (0000057511). S.Z. acknowledges the support of the China Postdoctoral Science Foundation through grant No. 2021M700248. T.L. acknowledges support from the National Natural Science Foundation of China (NSFC) through grants No. 12073061 and No. 12122307, the International Partnership Program of the Chinese Academy of Sciences (CAS) through grant No. 114231KYSB20200009, the Shanghai Pujiang Program (20PJ1415500), and science research grants from the China Manned Space Project with no. CMS-CSST-2021-B06. A.Z. thanks the support of the Institut Universitaire de France. M.J. acknowledges support from the Academy of Finland grant No. 348342. H.-L. Liu is supported by National Natural Science Foundation of China (NSFC) through the grant No.12103045. AS gratefully acknowledges support by the Fondecyt Regular (project code 1220610), and ANID BASAL projects ACE210002 and FB210003. L.B. gratefully acknowledges support by the ANID BASAL projects ACE210002 and FB210003. C.W.L. acknowledges the support by the BasicScience Research Program through the National Research

Foundation of Korea (NRF) funded by the Ministry of Education, Science and Technology (NRF-2019R1A2C1010851), and the support by the Korea Astronomy and Space Science Institute grant funded by the Korea government (MSIT) (Project No. 2022-1-840-05). This research was carried out in part at the Jet Propulsion Laboratory, which is operated by the California Institute of Technology under a contract with the National Aeronautics and Space Administration (80NM0018D0004).

This paper makes use of the following ALMA data: ADS/JAO.ALMA#2019.1.00685.S. ALMA is a partnership of ESO (representing its member states), NSF (USA), and NINS (Japan), together with NRC (Canada), MOST and ASIAA (Taiwan), and KASI (Republic of Korea), in cooperation with the Republic of Chile. The Joint ALMA Observatory is operated by ESO, AUI/NRAO, and NAOJ

DATA AVAILABILITY

The data underlying this article will be shared on the request to the corresponding author.

REFERENCES

- Anathpindika S., Bhatt H. C., 2012, *MNRAS*, **427**, 1713
- Anderson L. D., Bania T. M., Balser D. S., Cunningham V., Wenger T. V., Johnstone B. M., Armentrout W. P., 2014, *ApJS*, **212**, 1
- Avison A., et al., 2021, *A&A*, **645**, A142
- Bachiller R., Fuente A., Kumar M. S. N., 2002, *A&A*, **381**, 168
- Baug T., et al., 2018, *ApJ*, **852**, 119
- Baug T., et al., 2021, *MNRAS*, **507**, 4316
- Bertoldi F., 1989, *ApJ*, **346**, 735
- Bessell M. S., Brett J. M., 1988, *PASP*, **100**, 1134
- Beuther H., Linz H., Henning T., 2013, *A&A*, **558**, A81
- Beuther H., et al., 2016, *A&A*, **595**, A32
- Bisbas T. G., Wünsch R., Whitworth A. P., Hubber D. A., Walch S., 2011, *ApJ*, **736**, 142
- Bodenheimer P. H., 2011, Principles of Star Formation, doi:10.1007/978-3-642-15063-0.
- Bonnell I. A., Bate M. R., Clarke C. J., Pringle J. E., 2001, *MNRAS*, **323**, 785
- Bourke T. L., Hyland A. R., Robinson G., James S. D., Wright C. M., 1995, *MNRAS*, **276**, 1067
- Buslaeva A. I., Kirsanova M. S., Punanova A. F., 2021, *Astronomy Reports*, **65**, 488
- Carey S. J., et al., 2009, *PASP*, **121**, 76
- Chauhan N., Pandey A. K., Ogura K., Ojha D. K., Bhatt B. C., Ghosh S. K., Rawat P. S., 2009, *MNRAS*, **396**, 964
- Choudhury R., Mookerjee B., Bhatt H. C., 2010, *ApJ*, **717**, 1067
- Churchwell E., et al., 2006, *ApJ*, **649**, 759
- Churchwell E., et al., 2009, *PASP*, **121**, 213
- Contreras Y., et al., 2018, *ApJ*, **861**, 14
- Cuadrado S., Goicoechea J. R., Pilleri P., Cernicharo J., Fuente A., Joblin C., 2015, *A&A*, **575**, A82
- Cyganowski C. J., et al., 2008, *AJ*, **136**, 2391
- Cyganowski C. J., Brogan C. L., Hunter T. R., Churchwell E., 2009, *ApJ*, **702**, 1615
- Dale J. E., Ngoumou J., Ercolano B., Bonnell I. A., 2014, *MNRAS*, **442**, 694
- Dale J. E., Haworth T. J., Bressert E., 2015, *MNRAS*, **450**, 1199
- De Vries C. H., Myers P. C., 2005, *ApJ*, **620**, 800
- De Vries C. H., Narayanan G., Snell R. L., 2002, *ApJ*, **577**, 798
- Deharveng L., Zavagno A., Caplan J., 2005, *A&A*, **433**, 565
- Deharveng L., et al., 2012, *A&A*, **546**, A74
- Dempsey J. T., Thomas H. S., Currie M. J., 2013, *ApJS*, **209**, 8

- Dewangan L. K., Ojha D. K., Sharma S., Palacio S. d., Bhadani N. K., Das A., 2020, *ApJ*, **903**, 13
- Dodson R., Ojha R., Ellingsen S. P., 2004, *MNRAS*, **351**, 779
- Dunham M. M., Arce H. G., Mardones D., Lee J.-E., Matthews B. C., Stutz A. M., Williams J. P., 2014, *ApJ*, **783**, 29
- Duvert G., Cernicharo J., Bachiller R., Gomez-Gonzalez J., 1990, *A&A*, **233**, 190
- Elia D., et al., 2017, *MNRAS*, **471**, 100
- Estalella R., Anglada G., Díaz-Rodríguez A. K., Mayen-Gijón J. M., 2019, *A&A*, **626**, A84
- Faúndez S., Bronfman L., Garay G., Chini R., Nyman L. Å., May J., 2004, *A&A*, **426**, 97
- Feddersen J. R., et al., 2020, *ApJ*, **896**, 11
- Figueira M., Zavagno A., Bronfman L., Russeil D., Finger R., Schuller F., 2020, *A&A*, **639**, A93
- Fontani F., Caselli P., Crapsi A., Cesaroni R., Molinari S., Testi L., Brand J., 2006, *A&A*, **460**, 709
- Fuente A., Martín-Pintado J., Bachiller R., Neri R., Palla F., 1998, *A&A*, **334**, 253
- Fuente A., Martín-Pintado J., Bachiller R., Rodríguez-Franco A., Palla F., 2002, *A&A*, **387**, 977
- Fukuda N., Hanawa T., Sugitani K., 2002, *ApJ*, **568**, L127
- Fukuda N., Miao J., Sugitani K., Kawahara K., Watanabe M., Nakano M., Pickles A. J., 2013, *ApJ*, **773**, 132
- Fukushima H., Yajima H., Sugimura K., Hosokawa T., Omukai K., Matsumoto T., 2020, *MNRAS*, **497**, 3830
- Gaia Collaboration et al., 2021, *A&A*, **649**, A1
- Geen S., Soler J. D., Hennebelle P., 2017, *MNRAS*, **471**, 4844
- Getman K. V., Feigelson E. D., Luhman K. L., Sicilia-Aguilar A., Wang J., Garmire G. P., 2009, *ApJ*, **699**, 1454
- Ginsburg A., Mirocha J., 2011, PySpecKit: Python Spectroscopic Toolkit (ascl:1109.001)
- Goicoechea J. R., et al., 2016, *Nature*, **537**, 207
- Gómez-Ruiz A. I., Kurtz S. E., Araya E. D., Hofner P., Loinard L., 2016, *ApJS*, **222**, 18
- Gonzalez-Alfonso E., Cernicharo J., Radford S. J. E., 1995, *A&A*, **293**, 493
- González-Samaniego A., Vázquez-Semadeni E., 2020, *MNRAS*, **499**, 668
- Gritschneider M., Naab T., Burkert A., Walch S., Heitsch F., Wetzstein M., 2009a, *MNRAS*, **393**, 21
- Gritschneider M., Naab T., Walch S., Burkert A., Heitsch F., 2009b, *ApJ*, **694**, L26
- Haikala L. K., Olberg M., 2007, *A&A*, **466**, 191
- Haworth T. J., Harries T. J., Acreman D. M., 2012, *MNRAS*, **426**, 203
- Haworth T. J., Harries T. J., Acreman D. M., Rundle D. A., 2013, *MNRAS*, **431**, 3470
- Helfand D. J., Becker R. H., White R. L., Fallon A., Tuttle S., 2006, *AJ*, **131**, 2525
- Hildebrand R. H., 1983, *QJRAS*, **24**, 267
- Huggins P. J., Carlson W. J., Kinney A. L., 1984, *A&A*, **133**, 347
- Ikeda H., et al., 2008, *AJ*, **135**, 2323
- Imai R., Sugitani K., Miao J., Fukuda N., Watanabe M., Kusune T., Pickles A. J., 2017, *ApJ*, **845**, 99
- Ingallinera A., et al., 2014, *MNRAS*, **437**, 3626
- Kauffmann J., Bertoldi F., Bourke T. L., Evans N. J. I., Lee C. W., 2008, *A&A*, **487**, 993
- Kendrew S., et al., 2016, *ApJ*, **825**, 142
- Kessel-Deynet O., Burkert A., 2003, *MNRAS*, **338**, 545
- Kinnear T. M., Miao J., White G. J., Sugitani K., Goodwin S., 2015, *MNRAS*, **450**, 1017
- Kirk H., Myers P. C., Bourke T. L., Gutermuth R. A., Hedden A., Wilson G. W., 2013, *ApJ*, **766**, 115
- Kirsanova M. S., Punanova A. F., Semenov D. A., Vasyunin A. I., 2021, *MNRAS*, **507**, 3810
- Koch E. W., Rosolowsky E. W., 2015, *MNRAS*, **452**, 3435
- Krumholz M. R., 2017, Star Formation, doi:10.1142/10091.
- Krumholz M. R., Klein R. I., McKee C. F., Offner S. S. R., Cunningham A. J., 2009, *Science*, **323**, 754
- Kumar M. S. N., Palmeirim P., Arzoumanian D., Inutsuka S. I., 2020, *A&A*, **642**, A87
- Lada C. J., Adams F. C., 1992, *ApJ*, **393**, 278
- Ladeyschikov D. A., Sobolev A. M., Parfenov S. Y., Alexeeva S. A., Bieging J. H., 2015, *MNRAS*, **452**, 2306
- Launhardt R., et al., 2010, *ApJS*, **188**, 139
- Lefloch B., Lazareff B., 1994, *A&A*, **289**, 559
- Lefloch B., Lazareff B., 1995, *A&A*, **301**, 522
- Lefloch B., Lazareff B., Castets A., 1997, *A&A*, **324**, 249
- Lequeux J., 2005, The Interstellar Medium, doi:10.1007/b137959.
- Li D., Kauffmann J., Zhang Q., Chen W., 2013, *ApJ*, **768**, L5
- Liu H.-L., Wu Y., Li J., Yuan J.-H., Liu T., Dong X., 2015, *ApJ*, **798**, 30
- Liu H.-L., et al., 2016, *ApJ*, **818**, 95
- Liu H.-L., et al., 2017a, *A&A*, **602**, A95
- Liu T., et al., 2017b, *ApJ*, **849**, 25
- Liu T., et al., 2020a, *MNRAS*, **496**, 2790
- Liu T., et al., 2020b, *MNRAS*, **496**, 2821
- Liu H.-L., et al., 2021a, *MNRAS*, **505**, 2801
- Liu X.-L., Xu J.-L., Wang J.-J., Yu N.-P., Zhang C.-P., Li N., Zhang G.-Y., 2021b, *A&A*, **646**, A137
- Liu H.-L., et al., 2022a, *MNRAS*, **510**, 5009
- Liu H.-L., et al., 2022b, *MNRAS*, **511**, 4480
- Löhr A., Bourke T. L., Lane A. P., Myers P. C., Parshley S. C., Stark A. A., Tothill N. F. H., 2007, *ApJS*, **171**, 478
- Lu X., Zhang Q., Liu H. B., Wang J., Gu Q., 2014, *ApJ*, **790**, 84
- Mackey J., Lim A. J., 2010, *MNRAS*, **403**, 714
- Maheswar G., Bhatt H. C., 2008, *Ap&SS*, **315**, 215
- Makai Z., Anderson L. D., Mascoop J. L., Johnstone B., 2017, *ApJ*, **846**, 64
- Mäkelä M. M., Haikala L. K., 2013, *A&A*, **550**, A83
- Manoj P., Bhatt H. C., Maheswar G., Muneer S., 2006, *ApJ*, **653**, 657
- Marsh K. A., et al., 2017, *MNRAS*, **471**, 2730
- Marshall B., Kerton C. R., 2019, *MNRAS*, **489**, 4809
- McKee C. F., Tan J. C., 2003, *ApJ*, **585**, 850
- McLeod A. F., Dale J. E., Ginsburg A., Ercolano B., Gritschneider M., Ramsay S., Testi L., 2015, *MNRAS*, **450**, 1057
- McMullin J. P., Waters B., Schiebel D., Young W., Golap K., 2007, CASA Architecture and Applications. p. 127
- Mège P., et al., 2021, *A&A*, **646**, A74
- Messineo M., et al., 2014, *A&A*, **569**, A20
- Meyer M. R., Calvet N., Hillenbrand L. A., 1997, *AJ*, **114**, 288
- Miao J., White G. J., Nelson R., Thompson M., Morgan L., 2006, *MNRAS*, **369**, 143
- Miao J., White G. J., Thompson M. A., Nelson R. P., 2009, *ApJ*, **692**, 382
- Miao J., Sugitani K., White G. J., Nelson R. P., 2010, *ApJ*, **717**, 658
- Milam S. N., Savage C., Brewster M. A., Ziurys L. M., Wyckoff S., 2005, *ApJ*, **634**, 1126
- Molinari S., et al., 2010, *PASP*, **122**, 314
- Mookerjee B., Sandell G., Güsten R., Riquelme D., Wiesemeyer H., Chambers E., 2019, *A&A*, **626**, A131
- Morgan L. K., Thompson M. A., Urquhart J. S., White G. J., Miao J., 2004, *A&A*, **426**, 535
- Morgan L. K., Thompson M. A., Urquhart J. S., White G. J., 2008, *A&A*, **477**, 557
- Motoyama K., Umemoto T., Shang H., 2007, *A&A*, **467**, 657
- Motoyama K., Umemoto T., Shang H., Hasegawa T., 2013, *ApJ*, **766**, 50
- Motte F., Bontemps S., Louvet F., 2018, *ARA&A*, **56**, 41
- Nagy Z., Ossenkopf V., Van der Tak F. F. S., Faure A., Makai Z., Bergin E. A., 2015, *A&A*, **578**, A124
- Nakatani R., Yoshida N., 2019, *ApJ*, **883**, 127
- Nielsen A. S., Olberg M., Knude J., Booth R. S., 1998, *A&A*, **336**, 329
- Niwa T., Tachihara K., Itoh Y., Oasa Y., Sunada K., Sugitani K., Mukai T., 2009, *A&A*, **500**, 1119
- Odenwald S., Fischer J., Lockman F. J., Stemwedel S., 1992, *ApJ*, **397**, 174
- Olano C. A., Walmsley C. M., Wilson T. L., 1994, *A&A*, **290**, 235
- Ortega M. E., Paron S., Giacani E., Rubio M., Dubner G., 2013, *A&A*, **556**, A105
- Ortega M. E., Giacani E., Paron S., Rubio M., 2016, *MNRAS*, **458**, 3684
- Ospina-Zamudio J., et al., 2019, *MNRAS*, **490**, 2679

- Ossenkopf V., Henning T., 1994, *A&A*, **291**, 943
- Padoan P., Pan L., Juvela M., Haugbølle T., Nordlund Å., 2020, *ApJ*, **900**, 82
- Palmeirim P., et al., 2017, *A&A*, **605**, A35
- Panwar N., Chen W. P., Pandey A. K., Samal M. R., Ogura K., Ojha D. K., Jose J., Bhatt B. C., 2014, *MNRAS*, **443**, 1614
- Paron S., Celis Peña M., Ortega M. E., Fariña C., Petriella A., Rubio M., Ashley R. P., 2017, *MNRAS*, **470**, 4662
- Patel N. A., Xie T., Goldsmith P. F., 1993, *ApJ*, **413**, 593
- Peretto N., et al., 2013, *A&A*, **555**, A112
- Peretto N., et al., 2020, *MNRAS*, **496**, 3482
- Pety J., Teyssier D., Fossé D., Gerin M., Roueff E., Abergel A., Habart E., Cernicharo J., 2005, *A&A*, **435**, 885
- Ramesh B., 1995, *MNRAS*, **276**, 923
- Ren Z., et al., 2021, *MNRAS*, **505**, 5183
- Rieke G. H., Lebofsky M. J., 1985, *ApJ*, **288**, 618
- Robitaille T. P., Whitney B. A., Indebetouw R., Wood K., Denzmore P., 2006, *ApJS*, **167**, 256
- Robitaille T. P., Whitney B. A., Indebetouw R., Wood K., 2007, *ApJS*, **169**, 328
- Rodríguez-Garza C. B., Kurtz S. E., Gómez-Ruiz A. I., Hofner P., Araya E. D., Kalenskii S. V., 2017, *ApJS*, **233**, 4
- Rosolowsky E. W., Pineda J. E., Kauffmann J., Goodman A. A., 2008, *ApJ*, **679**, 1338
- Saha P., Maheswar G., Ojha D. K., Baug T., Neha S., 2022, *MNRAS*, **515**, L67
- Sandford M. T. I., Whitaker R. W., Klein R. I., 1982, *ApJ*, **260**, 183
- Sanhueza P., Jackson J. M., Foster J. B., Garay G., Silva A., Finn S. C., 2012, *ApJ*, **756**, 60
- Schneider N., et al., 2016, *A&A*, **591**, A40
- Schuller F., et al., 2009, *A&A*, **504**, 415
- Sepúlveda I., et al., 2020, *A&A*, **644**, A128
- Serabyn E., Guesten R., Mundy L., 1993, *ApJ*, **404**, 247
- Sharma S., et al., 2016, *AJ*, **151**, 126
- Sharpless S., 1959, *ApJS*, **4**, 257
- Sicilia-Aguilar A., Patel N., Fang M., Roccatagliata V., Getman K., Goldsmith P., 2019, *A&A*, **622**, A118
- Solernó A., Areal M. B., Paron S., 2020, Boletín de la Asociación Argentina de Astronomía La Plata Argentina, **61B**, 130
- Stil J. M., et al., 2006, *AJ*, **132**, 1158
- Su Y., Yang J., Zhou X., Zhou P., Chen Y., 2014, *ApJ*, **796**, 122
- Sugitani K., Ogura K., 1994, *ApJS*, **92**, 163
- Sugitani K., Fukui Y., Mizuni A., Ohashi N., 1989, *ApJ*, **342**, L87
- Sugitani K., Fukui Y., Ogura K., 1991, *ApJS*, **77**, 59
- Sugitani K., Tamura M., Ogura K., 1995, *ApJ*, **455**, L39
- Sugitani K., Morita K.-I., Nakano M., Tamura M., Ogura K., 1997, *ApJ*, **486**, L141
- Szymczak M., Wolak P., Bartkiewicz A., 2015, *MNRAS*, **448**, 2284
- Teyssier D., Fossé D., Gerin M., Pety J., Abergel A., Roueff E., 2004, *A&A*, **417**, 135
- Thompson M. A., White G. J., Morgan L. K., Miao J., Fridlund C. V. M., Hultgren-White M., 2004a, *A&A*, **414**, 1017
- Thompson M. A., Urquhart J. S., White G. J., 2004b, *A&A*, **415**, 627
- Thompson M. A., Urquhart J. S., Moore T. J. T., Morgan L. K., 2012, *MNRAS*, **421**, 408
- Tobin J. J., Bos S. P., Dunham M. M., Bourke T. L., van der Marel N., 2018, *ApJ*, **856**, 164
- Tremblin P., et al., 2014, *A&A*, **568**, A4
- Umamoto T., et al., 2017, *PASJ*, **69**, 78
- Urquhart J. S., Thompson M. A., Morgan L. K., White G. J., 2004, *A&A*, **428**, 723
- Urquhart J. S., Thompson M. A., Morgan L. K., White G. J., 2006, *A&A*, **450**, 625
- Urquhart J. S., Thompson M. A., Morgan L. K., Pestalozzi M. R., White G. J., Muna D. N., 2007, *A&A*, **467**, 1125
- Urquhart J. S., Morgan L. K., Thompson M. A., 2009, *A&A*, **497**, 789
- Urquhart J. S., et al., 2014, *MNRAS*, **443**, 1555
- Urquhart J. S., et al., 2018, *MNRAS*, **473**, 1059
- Valdettaro R., Palla F., Brand J., Cesaroni R., 2005, *A&A*, **443**, 535
- Valdettaro R., Chapman J. M., Lovell J. E. J., Palla F., 2007, *A&A*, **466**, 247
- Valdettaro R., Migenes V., Trinidad M. A., Brand J., Palla F., 2008, *ApJ*, **675**, 1352
- Voronkov M. A., Caswell J. L., Ellingsen S. P., Green J. A., Breen S. L., 2014, *MNRAS*, **439**, 2584
- Walch S., Whitworth A. P., Bisbas T. G., Hubber D. A., Wunsch R., 2015, *MNRAS*, **452**, 2794
- Wang S., Looney L. W., 2007, *ApJ*, **659**, 1360
- Wang Z., Bovik A. C., Sheikh H. R., Simoncelli E. P., 2004, *IEEE Transactions on Image Processing*, **13**, 600
- Wang Y., et al., 2020, *A&A*, **634**, A83
- Watkins E. J., Peretto N., Marsh K., Fuller G. A., 2019, *A&A*, **628**, A21
- White G. J., et al., 1999, *A&A*, **342**, 233
- Whitworth A. P., Priestley F. D., 2021, *MNRAS*, **504**, 3156
- Whitworth A. P., Bhattal A. S., Chapman S. J., Disney M. J., Turner J. A., 1994, *MNRAS*, **268**, 291
- Wilson T. L., Rood R., 1994, *ARA&A*, **32**, 191
- Yuan J., et al., 2018, *ApJ*, **852**, 12
- Zavagno A., Pomarès M., Deharveng L., Hosokawa T., Russeil D., Caplan J., 2007, *A&A*, **472**, 835
- Zavagno A., et al., 2020, *A&A*, **638**, A7
- Zhang Y., et al., 2016, *ApJ*, **832**, 158
- Zhang S., et al., 2020, *A&A*, **637**, A40
- Zhang S., et al., 2021, *A&A*, **646**, A25
- Zhou S., Evans Neal J. I., Koempe C., Walmsley C. M., 1993, *ApJ*, **404**, 232
- Zinnecker H., Yorke H. W., 2007, *ARA&A*, **45**, 481
- de Villiers H. M., et al., 2014, *MNRAS*, **444**, 566
- van Dishoeck E. F., Blake G. A., 1998, *ARA&A*, **36**, 317

APPENDIX A: FIGURE INFORMATION

We list the detailed source information of Fig. 1 in Table A1. Meanwhile, we present two example maps that are used for identification of “ALMAGAL H II” and “ALMAGAL BRC” clumps in Figs A1 and A2, respectively.

Table A1: Source information of Figure 1.

Name	Catalog ^(a)	Mass ^(b) M _☉	Distance ^(c) kpc	Spatial Res. ^(d) pc	Angular Res. ^(d) "	Method ^(b)	Note ^(e)
SFO 01	SFO	2.18	0.85	0.06	14.0	SD+Continuum	Morgan et al. (2008)
SFO 02	SFO	3.37	0.85	0.06	14.0	SD+Continuum	Morgan et al. (2008)
SFO 03	SFO	1.15	0.85	0.06	14.0	SD+Continuum	Morgan et al. (2008)
SFO 04	SFO	2.0	0.19	0.05	54.0	SD+HCO ⁺	De Vries et al. (2002) ; Morgan et al. (2008)
SFO 05	SFO	25.85	1.9	0.13	14.0	SD+Continuum	Morgan et al. (2008) ; Fukuda et al. (2013)
SFO 07	SFO	31.26	1.9	0.13	14.0	SD+Continuum	Morgan et al. (2008)
SFO 09	SFO	3.03	1.9	0.13	14.0	SD+Continuum	Morgan et al. (2008)
SFO 10	SFO	2.22	1.9	0.13	14.0	SD+Continuum	Morgan et al. (2008)
SFO 11 SMM1	SFO	20.6	1.9	0.13	14.0	SD+Continuum	Thompson et al. (2004a)
SFO 11NE SMM1	SFO	13.4	1.9	0.13	14.0	SD+Continuum	Thompson et al. (2004a)
SFO 11E SMM1	SFO	18.7	1.9	0.13	14.0	SD+Continuum	Thompson et al. (2004a)
SFO 12	SFO	16.87	1.9	0.13	14.0	SD+Continuum	Morgan et al. (2008)
SFO 13	SFO	19.6	1.9	0.13	14.0	SD+Continuum	De Vries et al. (2002) ; Morgan et al. (2008)
SFO 14	SFO	51.79	1.9	0.13	14.0	SD+Continuum	Morgan et al. (2008)
SFO 15	SFO	7.04	3.4	0.23	14.0	SD+Continuum	Morgan et al. (2008)
SFO 16	SFO	1.25	0.4	0.03	14.0	SD+Continuum	De Vries et al. (2002) ; Morgan et al. (2008)
SFO 18	SFO	1.15	0.4	0.03	14.0	SD+Continuum	De Vries et al. (2002) ; Morgan et al. (2008)
SFO 20	SFO	6.0	0.4	0.1	54.0	SD+HCO ⁺	De Vries et al. (2002)
SFO 22	SFO	12.0	0.46	0.03	15.0	SD+ ¹³ CO	Motoyama et al. (2013)
SFO 23	SFO	6.26	1.6	0.11	14.0	SD+Continuum	Morgan et al. (2008)
SFO 25	SFO	55.0	0.78	0.2	54.0	SD+HCO ⁺	De Vries et al. (2002)
SFO 25a	SFO	5.59	0.78	0.05	14.0	SD+Continuum	Morgan et al. (2008)
SFO 25b	SFO	5.69	0.78	0.05	14.0	SD+Continuum	Morgan et al. (2008)
SFO 26	SFO	1.05	1.15	0.08	14.0	SD+Continuum	Morgan et al. (2008)
SFO 27	SFO	3.36	1.15	0.08	14.0	SD+Continuum	Morgan et al. (2008)
SFO 29	SFO	3.57	1.15	0.08	14.0	SD+Continuum	Morgan et al. (2008)
SFO 30	SFO	29.33	2.0	0.14	14.0	SD+Continuum	Morgan et al. (2008)
SFO 31	SFO	1.19	1.0	0.07	14.0	SD+Continuum	Morgan et al. (2008)
SFO 33	SFO	0.45	0.75	0.05	14.0	SD+Continuum	Morgan et al. (2008)
SFO 34	SFO	1.55	0.75	0.05	14.0	SD+Continuum	Morgan et al. (2008)
SFO 37	SFO	3.82	0.75	0.05	14.0	SD+Continuum	Sugitani et al. (1997) ; De Vries et al. (2002) ; Morgan et al. (2008)
SFO 39a	SFO	2.77	0.75	0.05	14.0	SD+Continuum	Morgan et al. (2008)
SFO 39b	SFO	2.09	0.75	0.05	14.0	SD+Continuum	Morgan et al. (2008)
SFO 40	SFO	0.45	0.75	0.05	14.0	SD+Continuum	Morgan et al. (2008)
SFO 41	SFO	0.43	0.75	0.05	14.0	SD+Continuum	Morgan et al. (2008)
SFO 42	SFO	0.89	0.75	0.05	14.0	SD+Continuum	Morgan et al. (2008)
SFO 43	SFO	28.34	2.4	0.16	14.0	SD+Continuum	Morgan et al. (2008)
SFO 58	SFO	10.0	0.7	0.11	32.0	SD+C ¹⁸ O	Urquhart et al. (2006)
SFO 68	SFO	66.0	1.7	0.26	32.0	SD+C ¹⁸ O	Urquhart et al. (2006)
SFO 75	SFO	177.0	2.8	0.43	32.0	SD+C ¹⁸ O	Urquhart et al. (2006, 2007)
SFO 76	SFO	48.0	1.8	0.28	32.0	SD+C ¹⁸ O	Urquhart et al. (2006)
SFO 79	SFO	51.0	1.35	0.21	32.0	SD+C ¹⁸ O	Urquhart et al. (2004)
SFO 87a	SFO	5.93	1.38	0.09	14.0	SD+Continuum	Morgan et al. (2008)
SFO 87b	SFO	4.45	1.38	0.09	14.0	SD+Continuum	Morgan et al. (2008)
SFO 89	SFO	5.18	1.38	0.09	14.0	SD+Continuum	Morgan et al. (2008)

Continued on next page

Table A1: Source information of Figure 1.

Name	Catalog ^(a)	Mass ^(b) M _⊙	Distance ^(c) kpc	Spatial Res. ^(d) pc	Angular Res. ^(d) "	Method ^(b)	Note ^(e)
CG1	CG	42.0	0.3	0.07	45.0	Extinction	Maheswar & Bhatt (2008); Mäkelä & Haikala (2013)
CG2	CG	31.0	0.3	0.07	45.0	Extinction	Maheswar & Bhatt (2008); Mäkelä & Haikala (2013)
CG3	CG	2.0	0.4	0.16	84.0	SD+NH ₃	Bourke et al. (1995); Maheswar & Bhatt (2008)
CG4	CG	50.0	0.2	0.04	45.0	SD+ ¹³ CO	Gonzalez-Alfonso et al. (1995); Maheswar & Bhatt (2008)
CG5	CG	0.2	0.4	0.16	84.0	SD+NH ₃	Bourke et al. (1995); Maheswar & Bhatt (2008)
CG6	CG	5.5	0.2	0.04	45.0	SD+ ¹³ CO	Gonzalez-Alfonso et al. (1995); Maheswar & Bhatt (2008)
CG7S	CG	85.0	1.9	0.2	22.0	SD+ ¹³ CO	Lefloch & Lazareff (1995); Maheswar & Bhatt (2008)
CG12	CG	100.0	0.63	0.07	24.0	SD+C ¹⁸ O	Haikala & Olberg (2007); Maheswar & Bhatt (2008)
CG13	CG	48.0	0.45	0.39	180.0	SD+ ¹³ CO	Löhr et al. (2007); Maheswar & Bhatt (2008)
CG14	CG	0.6	0.4	0.16	84.0	SD+NH ₃	Bourke et al. (1995); Maheswar & Bhatt (2008)
CG15	CG	0.8	0.4	0.16	84.0	SD+NH ₃	Bourke et al. (1995); Maheswar & Bhatt (2008)
CG16	CG	1.6	0.4	0.16	84.0	SD+NH ₃	Bourke et al. (1995); Maheswar & Bhatt (2008)
CG19	CG	0.9	0.4	0.16	84.0	SD+NH ₃	Bourke et al. (1995); Maheswar & Bhatt (2008)
CG20	CG	1.3	0.4	0.16	84.0	SD+NH ₃	Bourke et al. (1995); Maheswar & Bhatt (2008)
CG21	CG	0.2	0.4	0.16	84.0	SD+NH ₃	Bourke et al. (1995); Maheswar & Bhatt (2008)
CG22	CG	103.0	0.45	0.39	180.0	SD+ ¹³ CO	Löhr et al. (2007); Maheswar & Bhatt (2008)
CG24	CG	0.2	0.4	0.16	84.0	SD+NH ₃	Bourke et al. (1995); Maheswar & Bhatt (2008)
CG26	CG	1.3	0.4	0.16	84.0	SD+NH ₃	Bourke et al. (1995); Maheswar & Bhatt (2008)
CG27	CG	0.8	0.4	0.16	84.0	SD+NH ₃	Bourke et al. (1995); Maheswar & Bhatt (2008)
CG30	CG	58.0	0.45	0.39	180.0	SD+ ¹³ CO	Löhr et al. (2007); Maheswar & Bhatt (2008)
CG31	CG	16.5	0.45	0.09	43.0	SD+ ¹³ CO	Nielsen et al. (1998); Maheswar & Bhatt (2008)
CG32	CG	2.0	0.4				Maheswar & Bhatt (2008); Tobin et al. (2018)
CG34	CG	2.1	0.4	0.16	84.0	SD+NH ₃	Bourke et al. (1995); Maheswar & Bhatt (2008)
CG38	CG	0.6	0.45	0.09	43.0	SD+ ¹³ CO	Nielsen et al. (1998); Maheswar & Bhatt (2008)
GCD1	CG	8.7	0.4	0.16	84.0	SD+NH ₃	Bourke et al. (1995); Maheswar & Bhatt (2008)
GDC2	CG	3.0	0.4	0.16	84.0	SD+NH ₃	Bourke et al. (1995); Maheswar & Bhatt (2008)
GDC4	CG	1.1	0.4	0.16	84.0	SD+NH ₃	Bourke et al. (1995); Maheswar & Bhatt (2008)
GDC5	CG	5.8	0.4	0.16	84.0	SD+NH ₃	Bourke et al. (1995); Maheswar & Bhatt (2008)
Rosette-CG1	Individual	100.0	1.6	0.35	45.0	SD+ ¹³ CO	Patel et al. (1993)
Rosette-CG2	Individual	50.0	1.6	0.35	45.0	SD+ ¹³ CO	Patel et al. (1993)
Rosette-CG3	Individual	150.0	1.6	0.35	45.0	SD+ ¹³ CO	Patel et al. (1993)
Rosette-CG4	Individual	200.0	1.6	0.35	45.0	SD+ ¹³ CO	Patel et al. (1993)
Rosette-CG5	Individual	300.0	1.6	0.35	45.0	SD+ ¹³ CO	Patel et al. (1993)
Rosette-CG6	Individual	200.0	1.6	0.35	45.0	SD+ ¹³ CO	Patel et al. (1993)
Rosette-CG7	Individual	100.0	1.6	0.35	45.0	SD+ ¹³ CO	Patel et al. (1993)
Rosette-CG8	Individual	100.0	1.6	0.35	45.0	SD+ ¹³ CO	Patel et al. (1993)
Rosette-CG9	Individual	50.0	1.6	0.35	45.0	SD+ ¹³ CO	Patel et al. (1993)
W5-E-Pillars1	Individual	0.33	2.0	0.35	36.0	Herschel	Deharveng et al. (2012)
W5-E-Pillars2a	Individual	1.16	2.0	0.35	36.0	Herschel	Deharveng et al. (2012)
W5-E-Pillars2b	Individual	0.59	2.0	0.35	36.0	Herschel	Deharveng et al. (2012)
W5-E-Pillars2c	Individual	0.83	2.0	0.35	36.0	Herschel	Deharveng et al. (2012)
W5-E-Pillars3	Individual	0.97	2.0	0.35	36.0	Herschel	Deharveng et al. (2012)
W5-E-Pillars4	Individual	1.49	2.0	0.35	36.0	Herschel	Deharveng et al. (2012)
W5-E-Pillars5	Individual	0.47	2.0	0.35	36.0	Herschel	Deharveng et al. (2012)
W5-E-Pillars6a	Individual	1.38	2.0	0.35	36.0	Herschel	Deharveng et al. (2012)

Continued on next page

Table A1: Source information of Figure 1.

Name	Catalog ^(a)	Mass ^(b) M _⊙	Distance ^(c) kpc	Spatial Res. ^(d) pc	Angular Res. ^(d) "	Method ^(b)	Note ^(e)
W5-E-Pillars6b	Individual	1.38	2.0	0.35	36.0	Herschel	Deharveng et al. (2012)
W5-E-Pillars7a	Individual	0.96	2.0	0.35	36.0	Herschel	Deharveng et al. (2012)
W5-E-Pillars7b	Individual	1.09	2.0	0.35	36.0	Herschel	Deharveng et al. (2012)
W5-E-Pillars8	Individual	1.14	2.0	0.35	36.0	Herschel	Deharveng et al. (2012)
W5-E-Pillars9	Individual	2.46	2.0	0.35	36.0	Herschel	Deharveng et al. (2012)
W5-E-Pillars10	Individual	0.96	2.0	0.35	36.0	Herschel	Deharveng et al. (2012)
W5-E-Pillars11	Individual	0.44	2.0	0.35	36.0	Herschel	Deharveng et al. (2012)
W5-E-BRC1	Individual	55.0	2.0	0.15	15.6	SD+C ¹⁸ O	Niwa et al. (2009)
W5-E-BRC2	Individual	550.0	2.0	0.15	15.6	SD+C ¹⁸ O	Niwa et al. (2009)
W5-E-BRC3	Individual	67.0	2.0	0.15	15.6	SD+C ¹⁸ O	Niwa et al. (2009)
W5-E-BRC4	Individual	170.0	2.0	0.15	15.6	SD+C ¹⁸ O	Niwa et al. (2009)
W5-E-BRC5	Individual	110.0	2.0	0.15	15.6	SD+C ¹⁸ O	Niwa et al. (2009)
W5-E-BRC6	Individual	230.0	2.0	0.15	15.6	SD+C ¹⁸ O	Niwa et al. (2009)
W5-E-BRC7	Individual	740.0	2.0	0.15	15.6	SD+C ¹⁸ O	Niwa et al. (2009)
W5-E-BRC8	Individual	180.0	2.0	0.15	15.6	SD+C ¹⁸ O	Niwa et al. (2009)
W5-E-BRC9	Individual	130.0	2.0	0.15	15.6	SD+C ¹⁸ O	Niwa et al. (2009)
CygnusX-Globule1	Individual	1680.0	1.4	0.24	36.0	Herschel	Schneider et al. (2016)
CygnusX-Globule2	Individual	282.0	1.4	0.24	36.0	Herschel	Schneider et al. (2016)
CygnusX-Globule3	Individual	83.0	1.4	0.24	36.0	Herschel	Schneider et al. (2016)
CygnusX-Globule4	Individual	50.0	1.4	0.24	36.0	Herschel	Schneider et al. (2016)
CygnusX-Globule5	Individual	156.0	1.4	0.24	36.0	Herschel	Schneider et al. (2016)
CygnusX-Globule6	Individual	1403.0	1.4	0.24	36.0	Herschel	Schneider et al. (2016)
CygnusX-Globule7	Individual	86.0	1.4	0.24	36.0	Herschel	Schneider et al. (2016)
CygnusX-Pillars1	Individual	238.0	1.4	0.24	36.0	Herschel	Schneider et al. (2016)
CygnusX-Pillars2	Individual	108.0	1.4	0.24	36.0	Herschel	Schneider et al. (2016)
CygnusX-Pillars3	Individual	180.0	1.4	0.24	36.0	Herschel	Schneider et al. (2016)
CygnusX-Pillars4	Individual	1356.0	1.4	0.24	36.0	Herschel	Schneider et al. (2016)
LBN 131.54-08.16	Individual	200.0	2.0			Extinction	Maheswar & Bhatt (2008)
RNO 6	Individual	190.0	2.0	0.23	24.0	SD+ ¹³ CO	Bachiller et al. (2002); Maheswar & Bhatt (2008)
LDN 1616	Individual	180.0	0.4	0.12	60.0	SD+ ¹³ CO	Ramesh (1995); Maheswar & Bhatt (2008)
Sim 129	Individual	130.0	3.4			Extinction	Maheswar & Bhatt (2008)
LDN 1622	Individual	550.0	0.45			Extinction	Maheswar & Bhatt (2008)
Gal 96-15	Individual	215.0			22.0	SD+ ¹³ CO	Olano et al. (1994); Maheswar & Bhatt (2008)
Gal 110-13	Individual	85.0	0.44	0.12	55.0	SD+ ¹² CO	Odenwald et al. (1992); Maheswar & Bhatt (2008)
CB6	Individual	1.8	0.16	0.01	15.0	SD+Continuum	Launhardt et al. (2010); Maheswar & Bhatt (2008)
ORI-I-2	Individual	3.0	0.4	0.03	17.0	SD+ ¹³ CO	Sugitani et al. (1989)
IC1396-N	Individual	150.0	0.75	0.06	17.0	SD+ ¹³ CO	Sugitani et al. (1989)
L1206	Individual	95.0	0.91	0.08	17.0	SD+ ¹³ CO	Sugitani et al. (1989)
globule@IC 1396	Individual	20.0	0.75	0.07	20.0	SD+ ¹³ CO	Duvert et al. (1990)
IC 1396E	Individual	480.0	0.75	0.09	24.0	SD+CS	Serabyn et al. (1993)
BRC@Sh2-48	Individual	260.0	3.8	0.61	33.0	SD+Continuum	Ortega et al. (2013)
Most massive BRC@S233	Individual	90.0	2.3	0.52	47.0	SD+ ¹³ CO	Ladeyschikov et al. (2015)
BRC@CN20	Individual	5200.0	5.0	0.53	22.0	SD+ ¹³ CO	Ortega et al. (2016)
Pillar@G46.5-0.2	Individual	80.0	4.0	0.7	36.0	Herschel	Paron et al. (2017)
IC1396A	Individual	270.0	0.945	0.16	36.0	Herschel	Sicilia-Aguilar et al. (2019)

Continued on next page

Table A1: Source information of Figure 1.

Name	Catalog ^(a)	Mass ^(b) M _⊙	Distance ^(c) kpc	Spatial Res. ^(d) pc	Angular Res. ^(d) "	Method ^(b)	Note ^(e)
CG@Cep OB3	Individual	350.0	0.7	0.15	45.0	SD+ ¹³ CO	Marshall & Kerton (2019)
Tesure Chest	Individual	1000.0	2.3	0.32	29.0	SD+ ¹³ CO	Mookerjea et al. (2019)
BRC@N30	Individual	230.0	2.2	0.15	14.0	SD+C ¹⁸ O	Solernó et al. (2020)
Massive BRC@RCW120	Individual	200.0	1.34	0.12	19.0	SD+C ¹⁸ O	Figueira et al. (2020)
104080	ALMAGAL H II	2612	5.99	1.05	36.0	SD+Continuum	Urquhart et al. (2018), AGAL023.389+00.456
108768	ALMAGAL H II	9141	7.76	1.35	36.0	SD+Continuum	Urquhart et al. (2018), AGAL024.416+00.101
109047	ALMAGAL BRC	7798	7.76	1.35	36.0	SD+Continuum	Urquhart et al. (2018), AGAL024.459+00.197
110233	ALMAGAL H II	5521	6.04	1.05	36.0	SD+Continuum	Urquhart et al. (2018), AGAL024.673+00.151
111140	ALMAGAL BRC	408	6.03	1.05	36.0	SD+Continuum	Urquhart et al. (2018), AGAL024.849+00.086
112942	ALMAGAL BRC	841	3.34	0.58	36.0	SD+Continuum	Urquhart et al. (2018), AGAL025.224+00.289
115679	ALMAGAL H II	7031	8.68	1.51	36.0	SD+Continuum	Urquhart et al. (2018), AGAL025.736+00.211
115936	ALMAGAL BRC	5058	8.68	1.51	36.0	SD+Continuum	Urquhart et al. (2018), AGAL025.796+00.242
120828	ALMAGAL H II	243	4.42	0.77	36.0	SD+Continuum	Urquhart et al. (2018), AGAL026.956+00.076
126057	ALMAGAL BRC	2355	6.05	1.06	36.0	SD+Continuum	Urquhart et al. (2018), AGAL028.321+00.009
128280	ALMAGAL H II	631	4.71	0.82	36.0	SD+Continuum	Urquhart et al. (2018), AGAL028.834+00.209
133651	ALMAGAL BRC	1119	5.16	0.9	36.0	SD+Continuum	Urquhart et al. (2018), AGAL029.862+00.044
59542	ALMAGAL BRC	966	2.57	0.45	36.0	SD+Continuum	Urquhart et al. (2018), AGAL013.178+00.059
62842	ALMAGAL H II	774	3.1	0.54	36.0	SD+Continuum	Urquhart et al. (2018), AGAL014.019+00.134
704454	ALMAGAL BRC	1340	3.8	0.66	36.0	SD+Continuum	Urquhart et al. (2018), AGAL305.137+00.069
705424	ALMAGAL H II	883	3.8	0.66	36.0	SD+Continuum	Urquhart et al. (2018), AGAL305.307+00.039
705736	ALMAGAL BRC	1091	3.8	0.66	36.0	SD+Continuum	Urquhart et al. (2018), AGAL305.362+00.151
707313	ALMAGAL BRC	178	3.8	0.66	36.0	SD+Continuum	Urquhart et al. (2018), AGAL305.667+00.106
708358	ALMAGAL BRC	771	3.8	0.66	36.0	SD+Continuum	Urquhart et al. (2018), AGAL305.887+00.016
716353	ALMAGAL BRC	574	3.65	0.64	36.0	SD+Continuum	Urquhart et al. (2018), AGAL308.646+00.647
716713	ALMAGAL BRC	136	3.65	0.64	36.0	SD+Continuum	Urquhart et al. (2018), AGAL308.731+00.729
720116	ALMAGAL BRC	4207	6.25	1.09	36.0	SD+Continuum	Urquhart et al. (2018), AGAL309.534+00.741
730127	ALMAGAL BRC	141	3.42	0.6	36.0	SD+Continuum	Urquhart et al. (2018), AGAL312.039+00.082
737671	ALMAGAL BRC	403	4.23	0.74	36.0	SD+Continuum	Urquhart et al. (2018), AGAL314.237+00.417
737762	ALMAGAL H II	256	4.23	0.74	36.0	SD+Continuum	Urquhart et al. (2018), AGAL314.262+00.444
744757	ALMAGAL H II	1239	2.52	0.44	36.0	SD+Continuum	Urquhart et al. (2018), AGAL316.811+00.059
797087	ALMAGAL BRC	1633	3.98	0.69	36.0	SD+Continuum	Urquhart et al. (2018), AGAL330.674+00.376
799034	ALMAGAL H II	1774	5.3	0.93	36.0	SD+Continuum	Urquhart et al. (2018), AGAL331.061+00.166
800079	ALMAGAL BRC	583	5.3	0.93	36.0	SD+Continuum	Urquhart et al. (2018), AGAL331.242+00.201
800751	ALMAGAL BRC	920	3.98	0.69	36.0	SD+Continuum	Urquhart et al. (2018), AGAL331.342+00.347
807707	ALMAGAL BRC	1268	3.57	0.62	36.0	SD+Continuum	Urquhart et al. (2018), AGAL332.774+00.584
809185	ALMAGAL H II	705	3.57	0.62	36.0	SD+Continuum	Urquhart et al. (2018), AGAL333.001+00.436
813886	ALMAGAL H II	676	3.57	0.62	36.0	SD+Continuum	Urquhart et al. (2018), AGAL333.683+00.256
822761	ALMAGAL BRC	1936	3.31	0.58	36.0	SD+Continuum	Urquhart et al. (2018), AGAL335.789+00.174
826927	ALMAGAL BRC	685	5.03	0.88	36.0	SD+Continuum	Urquhart et al. (2018), AGAL336.573+00.109
834656	ALMAGAL H II	796	2.86	0.5	36.0	SD+Continuum	Urquhart et al. (2018), AGAL337.934+00.507
839208	ALMAGAL BRC	875	7.86	1.37	36.0	SD+Continuum	Urquhart et al. (2018), AGAL338.836+00.334
839678	ALMAGAL BRC	2104	4.16	0.73	36.0	SD+Continuum	Urquhart et al. (2018), AGAL338.926+00.634
876093	ALMAGAL BRC	7362	9.84	1.72	36.0	SD+Continuum	Urquhart et al. (2018), AGAL347.586+00.216
876288	ALMAGAL BRC	13552	9.84	1.72	36.0	SD+Continuum	Urquhart et al. (2018), AGAL347.627+00.149
G305.5393+00.3394	ALMAGAL H II	1531	3.8	0.66	36.0	SD+Continuum	Urquhart et al. (2018), AGAL305.539+00.339

Continued on next page

Table A1: Source information of Figure 1.

Name	Catalog ^(a)	Mass ^(b) M _⊙	Distance ^(c) kpc	Spatial Res. ^(d) pc	Angular Res. ^(d) "	Method ^(b)	Note ^(e)
S1	Simulation	2		0.015			Sandford et al. (1982) , resolution is grid size
S2	Simulation	20		0.008			Lefloch & Lazareff (1994) , most massive model
S3	Simulation	85		0.07			Lefloch & Lazareff (1995) , CG7S, single dish observation
S4	Simulation	40		0.1			Kessel-Deynet & Burkert (2003) , SPH simulation
S5	Simulation	30					Motoyama et al. (2007)
S6	Simulation	96					Gritschneider et al. (2009b) , SPH simulation
S7	Simulation	35					Miao et al. (2009) , SPH simulation, most massive model
S8	Simulation	68					Miao et al. (2010) , SPH simulation, the Eagle nebula
S9	Simulation	2					Miao et al. (2010) , SPH simulation, IC59
S10	Simulation	666					Mackey & Lim (2010) , elephant trunks in H II regions
S11	Simulation	15					Bisbas et al. (2011) , SPH simulation, most massive model
S12	Simulation	400					Anathpindika & Bhatt (2012) , SPH simulation
S13	Simulation	159		0.038			Haworth et al. (2012) , most massive model
S14	Simulation	185		0.012			Haworth et al. (2013) , most massive model
S15	Simulation	30					Kinnear et al. (2015) , SPH simulation
S16	Simulation	783					Walch et al. (2015) , SPH simulation, most massive clump

^(a) Source catalog. The types of sources described in Sect. 1. “Simulation” means the simulation work focusing on the RDI mechanism.

^(b) Methods of mass calculations. The “SD” means single-dish radio observations. The “Continuum” means that the molecular mass is derived from mm/submm dust continuum. The “*Herschel*” means that the mass is derived from *Herschel* far infrared emissions. The “Extinction” means that the mass is derived from optical extinction. HCO⁺, ¹³CO, C¹⁸O, and NH₃ indicate the molecules that are used to derive the mass with an assumed abundance.

^(c) Distance taken from corresponding references.

^(d) Spatial and angular resolution of the observations.

^(e) Corresponding references and some notable information.

APPENDIX B: ALMA AND OTHER OBSERVATIONAL DATA

B1 ALMA data

We made use of ATOMS Band 3 data (ALMA project: 2019.1.00685.S) observed with the main array and 7 m ACA. I18290 was observed on 31st, October, 2019 with the typical precipitable water vapor (PWV) of 3.2 and 5.2 mm for main array and 7 m ACA, respectively. The integration time is three and eight minutes for the main array and 7 m ACA, respectively.

The data reductions were conducted using Common Astronomy Software Applications 5.6 (CASA, McMullin et al. 2007). A total of eight spectral windows (SPWs) were configured to cover 11 commonly used spectral lines. The narrow spectral windows SPWs 1-6 are at the lower sideband in range of 86.31-89.2 GHz with a spectral resolution of 0.2–0.4 km s⁻¹, whereas the wide spectral windows SPWs 7 and 8 are at the upper sideband in the range of 97.52-99.39 GHz and 99.46-101.33 GHz, respectively. The SPWs 7-8 are used for continuum measurements considering that they have a broad bandwidth of 1.87 GHz with a spectral resolution of ~ 1.6 km s⁻¹.

The main array and 7 m ACA data are combined and then cleaned using CASA task TCLEAN with a natural weighting and a pixel size “cell” of 0.4'' (about one fifth of the synthesized beam ≈ 2.08'' × 1.77''). The maximum recovering scales are 20'' and 76'' for the main array and ACA data, respectively.

B2 Other observational data

Here we list basic information of the supplementary data used:

- *Spitzer* images which include the 4.5 μm and 8.0 μm images taken from GLIMPSE (Galactic Legacy Infrared Mid-Plane Survey Extraordinaire, Churchwell et al. 2009) and the 24 μm images taken from MIPS GAL (Multiband Imaging Photometer Galactic Plane Survey, Carey et al. 2009).

- *Herschel* PPMAP N_{H_2} and T_{dust} images. Marsh et al. (2017) use the point process mapping (PPMAP) techniques to fit dust emission SED with the *Herschel* infrared Galactic Plane Survey (Hi-GAL, Molinari et al. 2010) 70, 160, 250, 350, and 500 μm images. The PPMAP results in a resolution of 12'', much higher than the classical pixel-by-pixel SED fitting. The Hi-GAL PPMAP N_{H_2} and T_{dust} maps are presented in Fig. B1.

- CO and its isotope molecular spectral cubes. (1) *James Clerk Maxwell Telescope* (JCMT) CO, ¹³CO, and C¹⁸O $J = 3 - 2$ cubes. The ¹²CO $J = 3 - 2$ cube is from CO High-Resolution Survey (COHRS, Dempsey et al. 2013), with a spatial and velocity resolution of 16.6'' and 1 km s⁻¹, respectively. The ¹³CO and C¹⁸O $J = 3 - 2$ cubes are from de Villiers et al. (2014) observed by the JCMT project M07AU20 (PI: Mark Thompson). Their spatial resolution is similar to CO data but with a much higher velocity resolution (0.055 km s⁻¹). (2) The CO, ¹³CO, and C¹⁸O $J = 1 - 0$ cubes are taken from FUGIN (Umemoto et al. 2017) which is a Galactic plane survey mainly targeting on the first and third quadrants with a spatial and velocity resolution of 20'' and 1.3 km s⁻¹, respectively. The zeroth moment maps for these transitions are shown in Fig. B1. The spectra averaged in the ATLASGAL 870 μm clump region for CO and its isotope molecules are shown in Fig. B2.

- VLA NH₃ (1, 1) and (2, 2) inversion line cubes from Lu et al. (2014) who used VLA D and DnC array configurations to survey 62 high-mass star-forming regions. The spatial and velocity resolutions are around 5.1'' × 3.2'' and 0.6 km s⁻¹, respectively. The zeroth moment map for (1, 1) is shown in Fig. G1.

- The twenty-centimeter continuum image combined from New GPS (Galactic Plane Survey) + THOR (The HI/OH/Recombination line survey of the inner Milky Way, Beuther et al. 2016; Wang et al. 2020). New GPS 20 cm image is taken from the project MAGPIS (Multi-Array Galactic Plane Imaging Survey, Helfand et al. 2006) with a resolution of ~6.2'' × 5.4'' (VLA B configuration). The THOR 20 cm data has a resolution of 25'' (VLA C configuration). The THOR data have been combined with the VLA Galactic Plane Survey (VGPS, VLA D + Effelsberg, Stil et al. 2006) using the CASA task *feather*. To recover both extended and compact structures, we combined the New GPS data with the THOR data using *feather*, with *sdfactor* = 1. The flux of the combined 20 cm image is improved about 10% compared to the original New GPS data.

APPENDIX C: RIM AND IBL

C1 Bright rim extracted by Filfinder

Spine of the 8 μm rim is extracted using *Filfinder*² that is based on mathematical morphology (Koch & Rosolowsky 2015). *Filfinder* first creates a mask using a threshold and then generates spines for the mask region. The bright 8-μm point sources located at the head of BRC bias the extraction of spine by distorting the spine path. We simply remove these bright point sources when extracting the rim mask.

In the procedure of mask creation (*Filfinder* task *Filfinder2D.create_mask*), there are two parameters crucial to determine the shape and size of rim mask: (1) Global threshold (*glob_thresh*), the minimum intensity of the pixel included in the rim mask, is 129 MJy sr⁻¹ in our case. (2) Adaptive threshold (*adapt_thresh*), the expected width of the rim, is 0.18 pc in our case.

An overdense and warm layer associated with the 8-μm rim is revealed in *Panels a* and *b* of Fig. B1. We estimate the rim mass except for the central clump. To limit the rim region, we simply use the 8-μm mask created by *Filfinder* in the rim extraction process. We got a mass of ~ 1100 M_⊙ for the rim region, by extracting the rim's pixels in the PPMAP N_{H_2} map. A N_{H_2} background of ~ 9 × 10²¹ cm⁻² is removed in the integration.

C2 IBL calculations

The total pressure exerted by IBL (P_{ex}) is derived from the New GPS + THOR combined 20 cm continuum. Assuming that all ionizing photons are absorbed in IBL, the electron number density n_e and photon flux Φ can be estimated from 20 cm continuum. Following the widely used formulae that are originally from the BRC quantitative analysis of Lefloch et al. (1997) and then rearranged by Thompson et al. (2004b),

$$n_e = 122.2 \sqrt{\left(\frac{S_\nu}{\text{mJy}}\right) \left(\frac{T_e}{\text{K}}\right)^{0.35} \left(\frac{\nu}{\text{GHz}}\right)^{0.1} \left(\frac{\eta_{rclp}}{\text{pc}}\right)^{-1} \left(\frac{\Theta}{''}\right)^{-2}} \text{ cm}^{-3}, \quad (\text{C1})$$

$$\Phi = 1.24 \times 10^{10} \left(\frac{S_\nu}{\text{mJy}}\right) \left(\frac{T_e}{\text{K}}\right)^{0.35} \left(\frac{\nu}{\text{GHz}}\right)^{0.1} \left(\frac{\Theta}{''}\right)^{-2} \text{ cm}^{-2} \text{ s}^{-1}, \quad (\text{C2})$$

² <https://fil-finder.readthedocs.io/en/latest/>

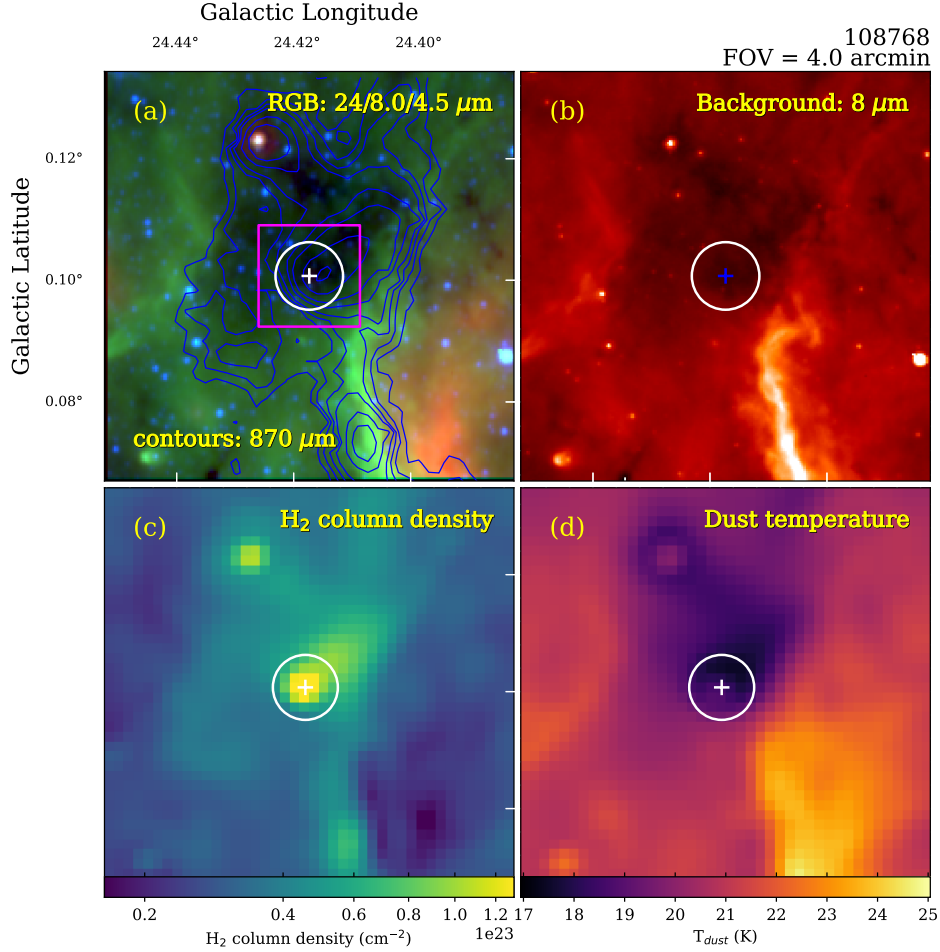


Figure A1. Example maps for identification of “ALMAGAL H II” source 108768. *Panel a:* *Spitzer* 24/8.0/4.5 μm RGB image overlaid with ATLASGAL 870 μm contours. The cross and circle present the ALMAGAL observation center and field of view, respectively. *Panel b:* 8 μm emission. *Panels c and d* shows the Hi-GAL PPMAP column density and dust temperature maps, respectively.

where S_ν is the integrated flux at frequency ν , Θ is the effective angular diameter over which the flux is integrated. There is no T_e measurement for our IBL and thus we simply estimate T_e using the empirical relation (Tremblin et al. 2014):

$$T_e = 278 \text{ K} \left(\frac{R_{\text{GC}}}{\text{kpc}} \right) + 6080 \text{ K}. \quad (\text{C3})$$

Bertoldi (1989) developed an approximate analytical solution for RDI model and found that the thickness of IBL is about ηr_{clp} with $\eta \sim 0.1$ to 0.2 for a wide range of parameter space. I18290 IBL is assumed to be the region enclosed by the 20 cm continuum contour of $\sim 2.38 \text{ mJy beam}^{-1}$ (40% of the 20 cm continuum peak value), resulting in a width of about 0.38 pc (15'') which is approximately in line with the analytical model. The resulting photon flux from the exciting OB cluster is $\Phi \simeq 1.8 \times 10^{10} \text{ cm}^{-2} \text{ s}^{-1}$, corresponding to a stellar photon rate of $\sim 4.8 \times 10^{51} \text{ s}^{-1}$. Note that the estimated photon rate has large uncertainties because (1) The interstellar absorption is ignored. (2) The initial separation between I18290 and the exciting OB cluster can be smaller than we observe now because of the rocket effect (Saha et al. 2022) and supernova events. (3) The projection effect leads to an underestimated separation.

Following Haworth et al. (2012), the mass loss rate due to photo-

evaporation could be estimated with

$$\dot{M}_{\text{eva}} = 4.4 \times 10^{-3} \left(\frac{\Phi}{\text{cm}^{-2} \text{ s}^{-1}} \right)^{0.5} \left(\frac{r_{\text{clp}}}{\text{pc}} \right)^{1.5} \text{ M}_\odot \text{ Myr}^{-1}, \quad (\text{C4})$$

We have $\dot{M}_{\text{eva}} \sim 680 \text{ M}_\odot \text{ Myr}^{-1}$. The remaining lifetime of the clump is $M_{\text{clp}}/\dot{M}_{\text{eva}} \simeq 2.1 \text{ Myr}$.

APPENDIX D: DENSITY AND MASS DERIVED FROM SPECTRA

Following the derivations in Zhang et al. (2016), the LTE column density dN/dv and the optically-thin LTE column density $dN/dv|_{\text{thin}}$ are correlated by:

$$\frac{dN}{dv} = \frac{dN}{dv}|_{\text{thin}} \frac{\tau_v}{1 - \exp(-\tau_v)}, \quad (\text{D1})$$

where τ_v is the optical depth at velocity v . This equation is derived based on the assumptions that the background temperature $T_{\text{bg}} = 2.7 \text{ K}$ is much smaller than the excitation temperature $T_{\text{ex}} (> 10 \text{ K})$ and the studied lines are at a frequency of about 80 to 110 GHz and have a line width of $< 100 \text{ km s}^{-1}$. Here, the column

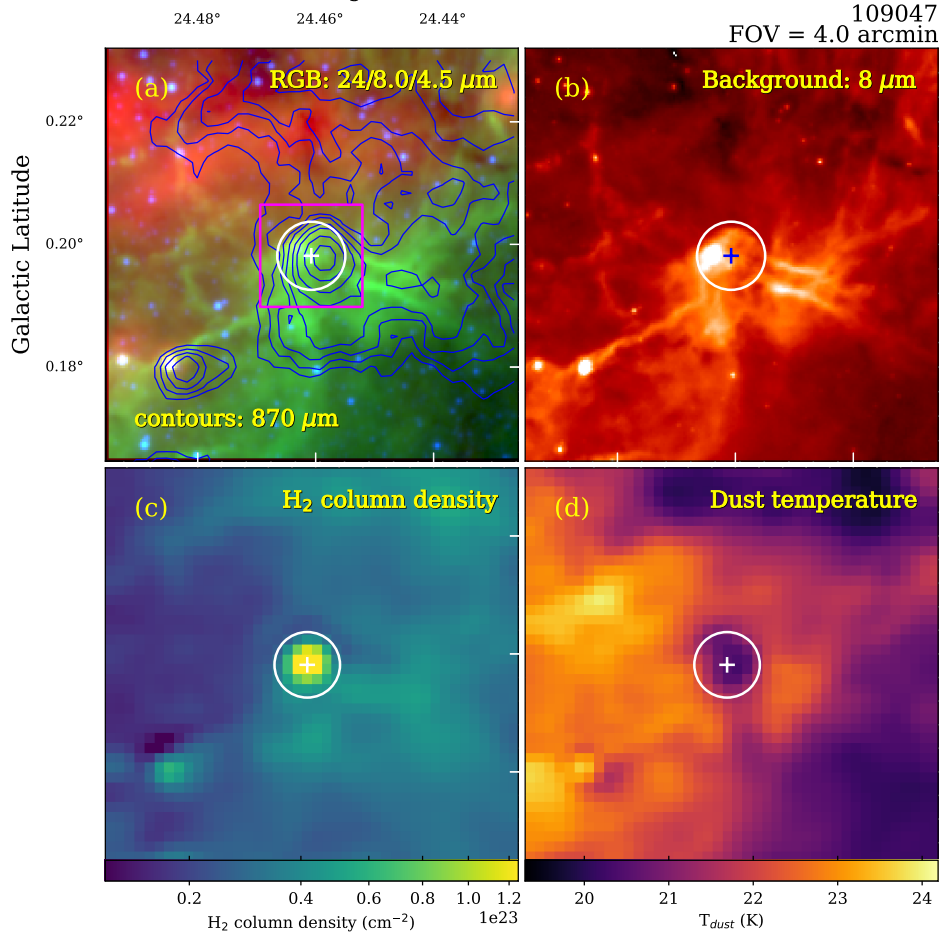


Figure A2. Example maps for identification of “ALMAGAL BRC” source 109047, similar to Fig. A1.

densities

$$\frac{dN}{dv} \approx \left(\frac{8\pi k_B \nu_{ul}^2}{hc^3 A_{ul} g_u R} \right) Q_{\text{rot}}(T_{\text{ex}}) \exp\left(\frac{E_u}{k_B T_{\text{ex}}}\right) \left(\frac{\tau_v}{1 - \exp(-\tau_v)} \right) \frac{T_r(v)}{f}, \quad (\text{D2})$$

$$\frac{dN}{dv}|_{\text{thin}} \approx \left(\frac{8\pi k_B \nu_{ul}^2}{hc^3 A_{ul} g_u R} \right) Q_{\text{rot}}(T_{\text{ex}}) \exp\left(\frac{E_u}{k_B T_{\text{ex}}}\right) \frac{T_r(v)}{f}, \quad (\text{D3})$$

where ν_{ul} , A_{ul} , R , f , T_r , Q_{rot} , E_u , and g_u , are the transition frequency, Einstein A coefficient, relative intensity of the hyperfine line, beam filling factor, radiation temperature, partition function, energy and degeneracy of the upper level, respectively.

In the following subsections, Eqs. D2 and D3 are used in our calculations of the clump mass, outflow properties, and CCH column density N_{CCH} .

D1 Clump mass

The kinematic distances of I18290 estimated by [Urquhart et al. \(2018\)](#) and [Mège et al. \(2021\)](#) are 5.34 kpc and 4.84 ± 0.27 kpc, respectively. In our work, a distance of 5.34 kpc with 10% error (0.53 kpc) is adopted. With this distance, [Urquhart et al. \(2018\)](#) derived a M_{clp}

of $\sim 1420 M_{\odot}$ by fitting SED from $8 \mu\text{m}$ to $870 \mu\text{m}$ with a two-components (warm and cold) gray-body function. [Lu et al. \(2014\)](#) derived a M_{clp} of $1400 M_{\odot}$ at this distance, using VLA NH_3 inversion lines with the abundance $[\text{NH}_3/\text{H}_2] = 3 \times 10^{-8}$.

The clump-averaged spectra of CO show complicated profiles compared to those of ^{13}CO and C^{18}O and thus we use $J = 1 - 0$ transitions of ^{13}CO and C^{18}O to probe the mass with moderate density and temperature. Assuming two isotopologues I_1 and I_2 have the same T_{ex} and f , rewriting and combining the radiation transfer formulae for I_1 and I_2 :

$$T_r(v) = f [J_v(T_{\text{ex}}) - J_v(T_{\text{bg}})] (1 - \exp(-\tau_v)), \quad (\text{D4})$$

$$J_v(T) = \frac{hv/k_B}{\exp\left(\frac{hv}{k_B T}\right) - 1}, \quad (\text{D5})$$

and then we have

$$\frac{T_{r,\text{I}_1}(v)}{T_{r,\text{I}_2}(v)} = \frac{1 - \exp(-\tau_{v,\text{I}_1})}{1 - \exp(-\tau_{v,\text{I}_2})}. \quad (\text{D6})$$

Further assuming that $\text{C}^{18}\text{O } J = 1 - 0$ is optically thin and $\text{I}_1 = ^{13}\text{CO}$, $\text{I}_2 = \text{C}^{18}\text{O}$, we have

$$\frac{T_{r,^{13}\text{CO}}(v)}{T_{r,\text{C}^{18}\text{O}}(v)} = \frac{1 - \exp(-\tau_{v,^{13}\text{CO}})}{\tau_{v,\text{C}^{18}\text{O}}} \approx \chi^{^{13}\text{CO}/\text{C}^{18}\text{O}} \frac{1 - \exp(-\tau_{v,^{13}\text{CO}})}{\tau_{v,^{13}\text{CO}}},$$

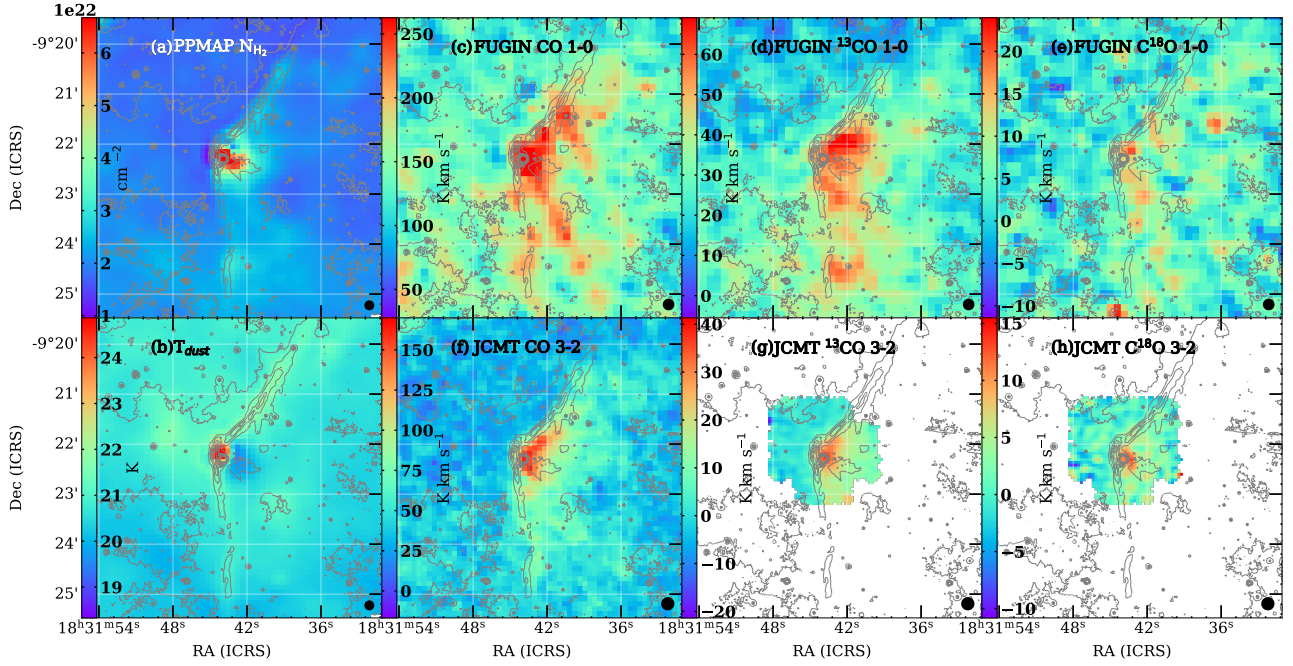


Figure B1. Hi-GAL PPMAP maps, CO and its isotope molecular emission. *Panels a and b:* PPMAP column density and dust temperature maps, respectively. *Panels c to e:* FUGIN CO, ^{13}CO , and C^{18}O $J = 1 - 0$ zeroth moment maps. *Panels f to h:* JCMT CO, ^{13}CO , and C^{18}O $J = 3 - 2$ zeroth moment maps. The gray contours represent the $8\ \mu\text{m}$ emission with levels of $[1, 1.5, 2, 2.5, 3, 3.5, 4, 4.5] \times 100\ \text{MJy sr}^{-1}$.

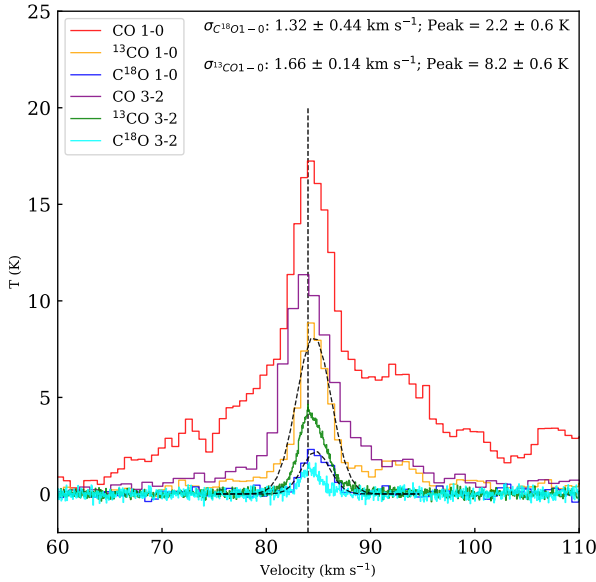


Figure B2. Clump-averaged spectra observed by JCMT and Nobeyama. The Gaussian fittings to ^{13}CO and C^{18}O $J = 1 - 0$ are shown as black dashed lines.

(D7)

where abundance ratio $\chi_{^{13}\text{CO}/^{18}\text{O}}$ can be estimated from isotope ratio gradients (Wilson & Rood 1994; Milam et al. 2005)

$$[^{16}\text{O}/^{18}\text{O}] = 58.8R_{\text{GC}} + 37.1, [^{12}\text{C}/^{13}\text{C}] = 7.5R_{\text{GC}} + 7.6. \quad (\text{D8})$$

Therefore, τ_v and associated N can be solved with Eqs. D7 and D2, respectively. To reduce noise in the τ_v calculation, we follow the optical depth correction methods usually used in the protostellar outflows

(e.g. Dunham et al. 2014; Feddersen et al. 2020). The temperature ratio $T_{r,^{13}\text{CO}}(v)/T_{r,\text{C}^{18}\text{O}}(v)$ is fitted with a parabola function for channels with high signal-to-noise (SN) ratio and then $\tau_{r,^{13}\text{CO}}(v)$ is derived from this parabola according to Eq. D7. The maximum τ_v is ~ 1.5 at $85\ \text{km s}^{-1}$. With Eq. D8 and CO abundance (Fontani et al. 2006)

$$\chi_{\text{CO}} = 9.5 \times 10^{-5} \exp(1.105 - 0.13R_{\text{GC}}), \quad (\text{D9})$$

and adopting $\nu_{ul} = 110.201\ \text{GHz}$, $g_u = 2 \times 1 + 1 = 3$, $A_{ul} = 6.332 \times 10^{-8}\ \text{s}^{-1}$, $E_u = 5.29\ \text{K}$, $R = 1$, and $T_{\text{ex}} = 18\ \text{K}$ for ^{13}CO $J = 1 - 0$, we have $M_{\text{clp}} \simeq 1450\ M_{\odot}$ and $N_{\text{H}_2} \sim 1.72 \times 10^{22}\ \text{cm}^{-2}$ for I18290, which are a factor of 1.6 compared to the ones without optical depth correction.

D2 Outflow mass and properties

Among the ATOMS-observed spectra, $J = 1 - 0$ spectra of HCO^+ and H^{13}CO^+ are used to probe outflow properties. Following the optical depth corrections in Appendix D1 and assuming that H^{13}CO^+ $J = 1 - 0$ is optically thin, the optical depth τ_{v,HCO^+} of outflow HCO^+ $J = 1 - 0$ emission could be corrected to some extent. First, a cube of the temperature ratio $T_{r,\text{HCO}^+}(v)/T_{r,\text{H}^{13}\text{CO}^+}(v)$ is generated for the voxels with SN ratio larger than two in both HCO^+ and H^{13}CO^+ . The mean temperature ratios for each channel are calculated when that channel has more than five valid voxels. Then, a parabola fitting is applied on the mean temperature ratios of all valid channels. We set $\nu_{ul} = 89.1885247\ \text{GHz}$, $g_u = 2 \times 1 + 1 = 3$, $A_{ul} = 4.187 \times 10^{-5}\ \text{s}^{-1}$, $E_u = 4.28\ \text{K}$, and $R = 1$ for HCO^+ $J = 1 - 0$. The T_{ex} of HCO^+ $J = 1 - 0$ is set as $50\ \text{K}$, similar to the ALMA outflow survey towards HMSF regions carried out by Baug et al. (2021). Dunham et al. (2014) propose that a variation of T_{ex} from 10 to $50\ \text{K}$ could cause to a maximum variation in outflow parameters by a factor of one to three.

We adopt abundance $[\text{HCO}^+/\text{H}_2] = 5 \times 10^{-9}$, which is the typical value in the protostellar outflows revealed by Ospina-Zamudio et al. (2019). Note that HCO^+ abundance is enhanced in the outflow region and its variation can reach one magnitude even between different lobes of the same outflow. The outflow mass and its related parameters could be reduced to one fourth of the initial values if we use $[\text{HCO}^+/\text{H}_2] = 2 \times 10^{-8}$ that is the upper abundance detected by Ospina-Zamudio et al. (2019). Another uncertainty is that $\text{H}^{13}\text{CO}^+ J = 1 - 0$ could be optically thick around systematic velocity for dense cores, as the spectra shown in Fig. 5. Therefore, the derived outflow parameters could be underestimated on this point. A series of outflow parameters calculated based on channel-by-channel counting are listed in Table D1.

D3 CCH column density

Here we derive CCH column density N_{CCH} from CCH $N_{J,F} = 1_{3/2,2} - 0_{1/2,1}$ following Sanhueza et al. (2012) and Buslaeva et al. (2021). The rotational energy levels of CCH are described by rotational quantum number N rather than J . The relative intensity of hyperfine line $R = 1.66/4.0$ because we only use one of the six hyperfine lines of $N = 1 - 0$ (Sanhueza et al. 2012). The PDR should have a higher temperature compared to the clump body, here we test $T_{\text{ex}} = 60, 120, 180, \text{ and } 240 \text{ K}$ for optically thin case using Eq. D3. Setting $\nu_{ul} = 87.317 \text{ GHz}$, $g_u = 5$, $A_{ul} = 1.527 \times 10^{-6} \text{ s}^{-1}$, $E_u = 4.19 \text{ K}$, we have median N_{CCH} of 2.8 to $13 \times 10^{14} \text{ cm}^{-2}$ and 1.9 to $8.9 \times 10^{14} \text{ cm}^{-2}$ for the compressed and PeF components, respectively.

APPENDIX E: CORE AND YSO CANDIDATES

E1 Core extraction by Astrodendro

The dense cores are extracted in the cleaned main array + 7 m ACA combined continuum image (uncorrected with primary beam to have a uniform noise field) using Astrodendrograms³ (Rosolowsky et al. 2008). The extracted cores are “leaves” which do not have substructure in the dendrogram. The intensity threshold and the steps to differentiate the leaves are set as 4.5 rms and 0.5 rms, respectively. The minimum size considered as an independent leaf is half of the synthesized beam. Table E1 lists the primary beam-corrected properties for the extracted cores.

Assuming that dust continuum is optically thin, the core mass is (Hildebrand 1983)

$$M_{\text{core}} = R_{\text{gd}} \frac{S_{\nu} D^2}{\kappa_{\nu} B_{\nu}(T_{\text{dust}})}, \quad (\text{E1})$$

where S_{ν} is the flux corrected by the primary beam, $B_{\nu}(T_{\text{dust}})$ is the Planck function at frequency ν and T_{dust} . The gas-to-dust mass ratio R_{gd} is set as 100 in our case. The dust opacity per gram $\kappa_{\nu} = 0.18 \text{ cm}^2 \text{ g}^{-1}$, corresponding to the opacity of dust grains with thin ice mantles at a gas density of $\sim 10^6 \text{ cm}^{-3}$ (Ossenkopf & Henning 1994; Liu et al. 2020a). The S_{ν} errors are derived by multiplying image rms with core area. The combined errors of $R_{\text{gd}}/\kappa_{\nu}$ are $\sim 30\%$ (see Zhang et al. 2021 and references therein).

The T_{dust} is assumed to be equal to NH_3 kinetic temperature T_{kin} (Lu et al. 2014). The T_{kin} uncertainty of core is simply set as the value range of the pixels' T_{kin} in one VLA beam. Core masses for the lowest and highest T_{kin} are estimated ($M_{\text{core}}^{\text{cold}}$ and $M_{\text{core}}^{\text{warm}}$). The

differences between M_{core} and $M_{\text{core}}^{\text{cold}}$ or $M_{\text{core}}^{\text{warm}}$ are typically less than 20%, except for C1.

We also estimate core mass surface density $\Sigma_{\text{core}} = M_{\text{core}}/\pi r_{\text{core}}^2$, number density n_{H_2} , and column density N_{H_2} with the assumptions of a spherical shape and a molecular weight per hydrogen molecule $\mu_{\text{H}_2} = 2.8$ (Kauffmann et al. 2008).

E2 Classification of candidate YSOs

We classify candidate YSOs in a square region centered at RA = $18^{\text{h}}31^{\text{m}}43.23^{\text{s}}$, DEC = $-9^{\circ}22'28.5''$ with a width of $1.3'$, using the 2MASS and GLIMPSE point source catalogs (2MASS All-Sky Point Source Catalog and GLIMPSE I Spring 07 Archive), including bands 2MASS J, H, K_S and IRAC 3.6, 4.5, 5.8, and $8.0 \mu\text{m}$. There are fifty-one 2MASS and sixty-seven GLIMPSE point sources in this field. Gaia measurements are available for 41 and 35 of them, respectively. Most of the derived Gaia distances for them are $< 3 \text{ kpc}$. We make use of three relatively independent methods to extract candidate YSOs from the source catalogs: (1) 2MASS $H - K_S$ vs $J - H$ color-color criteria. The 2MASS color-color diagram (CCD) is able to quantify the infrared excess caused by circumstellar grains re-radiation. The candidate YSOs could be classified by comparing colors of the observed sources and a series of loci for different types of stars (main sequence, HAeBe, giant stars, and classical T Tauri (CTTS) stars). Figure E1 shows the $H - K_S$ vs $J - H$ CCD and the mentioned loci. The three gray dashed lines in Fig. E1 mark the regimes of Class I, Class II, and Class III (or field) stars from right to left. Several 2MASS-selected YSOs are likely to follow the loci of HAeBe stars, such as YSOs #1, 2, 6, and 11. (2) GLIMPSE color-color criteria. We follow the procedures proposed by Wang & Looney (2007) which extract YSOs based on $J - [3.6]$ vs $K_S - [4.5]$ CCD. These authors initially used it to extract YSOs around HAeBe stars. Only one candidate (YSO #7) is extracted with this method. (3) YSO SED modelling. By fitting YSO SED models⁴ of Robitaille et al. (2007) for the 31 point sources (20 of them have Gaia measurements) with more than three valid photometric measurements in 2MASS and GLIMPSE bands, only two YSOs (YSOs #7 and 8) are extracted.

Note that we possibly miss a number of potential YSOs due to bright and diffuse emission of the rim which causes some GLIMPSE sources, such as YSOs #9, 10, and 11, to lack valid photometric measurements and leads to a failure in SED fitting or color-color selection. YSO #11 is not included in GLIMPSE catalog though its $8 \mu\text{m}$ emission is the strongest in I18290. The Gaia parallax for YSO #11 (Gaia DR3 id: 4155952506159262592) is $0.818 \pm 0.367 \text{ mas}$, corresponding to $1.22^{+1.0}_{-0.38} \text{ kpc}$, and therefore it is just a foreground source.

APPENDIX F: CORE SPECTRA AND INFALL ESTIMATION

F1 Core spectra

Figures F1 to F3 show the ATOMS spectra for cores C1, C4 and C5, respectively. The averaged spectra extracted from semi-axis, double semi-axes, and triple semi-axes areas of core have no significant difference for high velocity resolution spectra such as $\text{HCO}^+ J = 1 - 0$. The $J = 1 - 0$ spectral profiles of HCO^+ and H^{13}CO^+ show red asymmetries for C1 and C4 while those of C3, C5, and possible C2 show blue asymmetries.

³ <https://dendrograms.readthedocs.io/en/stable/>

⁴ <https://sedfitter.readthedocs.io/en/stable/>

Table D1. Main outflow properties

Lobe	$M_{\text{out}}^{(a)}$ M_{\odot}	$P_{\text{out}}^{(a)}$ $M_{\odot} \text{ km s}^{-1}$	$E_{\text{out}}^{(a)}$ $M_{\odot} \text{ km}^2 \text{ s}^{-2}$	$\dot{M}_{\text{out}}^{(b)}$ $M_{\odot} \text{ kyr}^{-1}$	$\dot{P}_{\text{out}}^{(c)}$ $M_{\odot} \text{ km s}^{-1} \text{ kyr}^{-1}$	$\dot{E}_{\text{out}}^{(c)}$ L_{\odot}	$t_{\text{out}}^{(d)}$ kyr	$l_{\text{out}}^{(e)}$ pc	PA $^{(f)}$ °	OA $^{(g)}$ °	Velocity Range $^{(h)}$ km s $^{-1}$
Red	12	48	112	0.66	2.6	1.0	18.4	0.20	-145	88	86.75-95.25
Blue	10	47	139	0.54	2.6	1.3	17.9	0.24	52	102	70.75-81.50
Overall	22	95	251	1.2	5.2	2.3	18.2	0.22			
Thick/Thin $^{(i)}$	2	1.7	1.4	2.0	1.7	1.4					

$^{(a)}$ Total outflow mass, momentum, and energy derived from the sum of outflow mass, momentum, and energy of all included channels, respectively.

$M_{\text{out}} = \sum M_v$, $P_{\text{out}} = \sum (M_v \times v)$, and $E_{\text{out}} = \sum (1/2 M_v \times v^2)$.

$^{(b)}$ Outflow mass rate $\dot{M}_{\text{out}} = M_{\text{out}}/t_{\text{out}}$, here t_{out} is the kinematic age presented in the eighth column.

$^{(c)}$ Mechanical force $\dot{P}_{\text{out}} = P_{\text{out}}/t_{\text{out}}$ and mechanical luminosity $\dot{E}_{\text{out}} = E_{\text{out}}/t_{\text{out}}$, respectively.

$^{(d)}$ Kinematic age $t_{\text{out}} = l_{\text{out}}/v_{\text{max}}$, here v_{max} and l_{out} are the maximum outflow velocity and length, respectively.

$^{(e)}$ Outflow length l_{out} , derived from the 90th percentile of the outflow maximum length of all included channels.

$^{(f)}$ Position angle PA, derived from the median of PA for all included channels. The PA of one channel is the median PA of all outflow voxels in that channel.

$^{(g)}$ Opening angle OA, derived from median OA of all channels. The OA of one channel is derived from FWHM of OA distribution of all outflow voxels in that channel.

$^{(h)}$ Velocity ranges that outflow parameters are integrated and counted.

$^{(i)}$ Value ratios of optically thick calculations to optically thin calculations.

Table E1. Astrodendrogram results for combined images.

Core $^{(a)}$	RA °	DEC °	major $^{(b)}$ "	minor $^{(b)}$ "	PA °	$r_{\text{core}}^{(b)}$ "	$S^{(c)}$ mJy	$S_p^{(c)}$ mJy beam $^{-1}$	SN ratio
C1	277.9339	-9.3701	0.96	0.79	100.4	0.87	7.76±0.37	6.3±0.11	21.1
C2	277.9279	-9.3742	1.13	0.74	150.2	0.92	2.25±0.27	1.7±0.08	8.5
C3	277.9303	-9.3739	0.62	0.52	-179.6	0.57	1.91±0.09	2.5±0.08	22.3
C4	277.9337	-9.3716	1.04	0.53	128.9	0.74	1.18±0.14	0.98±0.10	8.6
C5	277.9296	-9.3737	0.38	0.31	-178.6	0.34	0.55±0.03	1.7±0.08	17.9

$^{(a)}$ Cores are ranked with their mass.

$^{(b)}$ Major and minor semi-axes, and equivalent radius, respectively.

$^{(c)}$ S and S_p are the primary beam corrected integrated flux and pixel maximum flux, respectively.

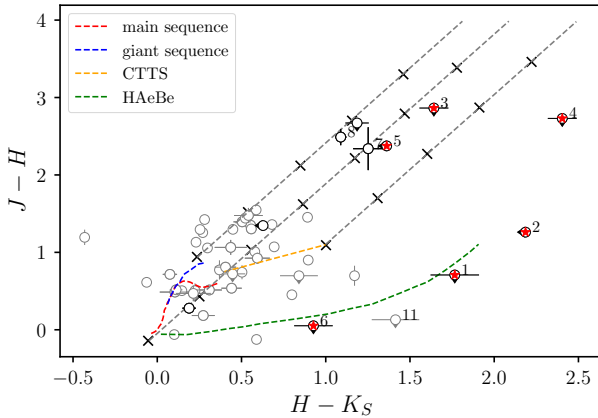


Figure E1. 2MASS color-color diagram. The loci of the main sequence, giants, CTTS, and H AeBe are taken from Bessell & Brett (1988), Lada & Adams (1992), and Meyer et al. (1997). The gray parallel lines are the reddening vectors from Rieke & Lebofsky (1985), with crosses marking the intervals of 5 mag visual extinction. The dots with the gray and black colors represent the 2MASS sources which are projected and (possibly) associated sources according to the Gaia measurements, respectively. The numbers mark the sources listed in Table 2. The red stars highlight the 2MASS-selected YSOs.

Figure F4 shows the ATOMS wide spectral windows SPW7 and SPW8 of core C2. The red lines highlight the spectra shown in

Fig. 4. Non detection for the warm tracer spectra suggests the cold and probably prestellar nature of core C2.

F2 Infall velocity estimation

Infall analyses are done using the Hill15⁵ model in pyspeckit. A total of five free parameters are fitted to the model: line peak T_{peak} , velocity dispersion σ , optical depth τ , systematic velocity v_{lsr} , and infall velocity v_{infall} . The Hill15 models perform well when there are two distinct peaks. We first fit $\text{HCO}^+ J = 1 - 0$ profiles for C2, C3, and C5. The fitted profiles are shown in cyan lines in Figs. 4, 5, and F3. The secondary peaks at the red-shifted side are poorly fitted for C3 and C5 due to the significant outflow wings. Therefore, we extract v_{infall} from $\text{H}^{13}\text{CO}^+ J = 1 - 0$ for C3 and C5. The fitted v_{infall} and velocity dispersion are listed in Table F1. The HCO^+ -derived v_{infall} is larger than H^{13}CO^+ -derived v_{infall} , consistent with the analyses of De Vries & Myers (2005) which propose that a more optically thin tracer may underestimate actual v_{infall} .

To further test the stability of Hill15 model fitting, we fit $\text{H}^{13}\text{CO}^+ J = 1 - 0$ profiles pixel-by-pixel for pixels with $\text{HCO}^+ J = 1 - 0$ peak > 2 K. The fitting results are shown in Fig. F5. Most valid pixels are located in the C3 region and the resulted v_{infall} and its error are stable at 0.5 km s^{-1} and 0.2 km s^{-1} , respectively. The pixel-by-pixel fitting shows that there is no significant difference for the modelled v_{infall} between core-averaged profile and pixel profile.

⁵ https://pyspeckit.readthedocs.io/en/latest/hill15infall_model.html

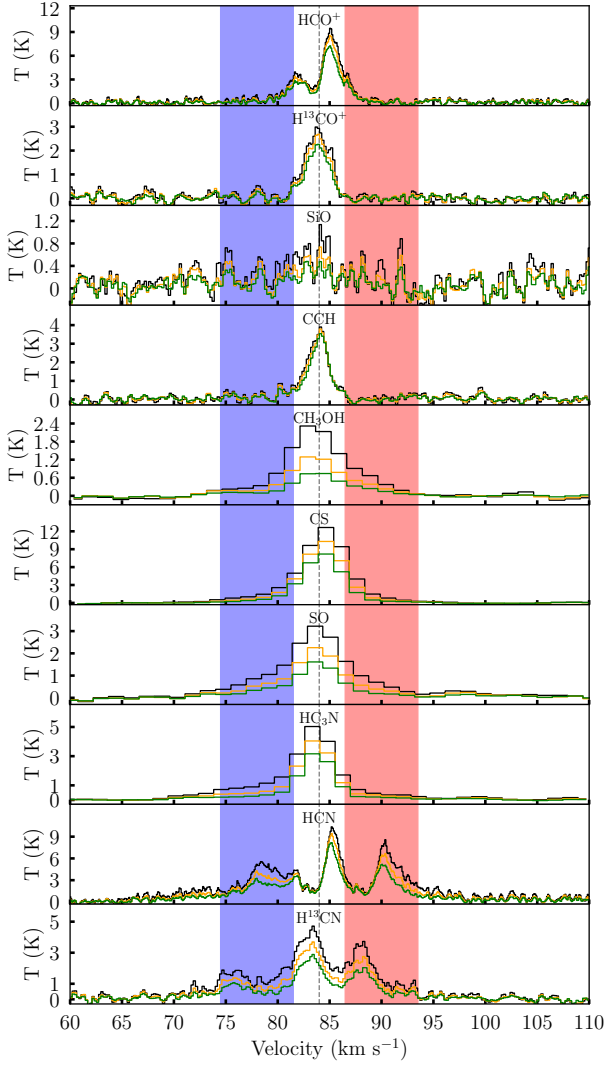


Figure F1. C1 ATOMS spectra. Similar to Fig. 4.

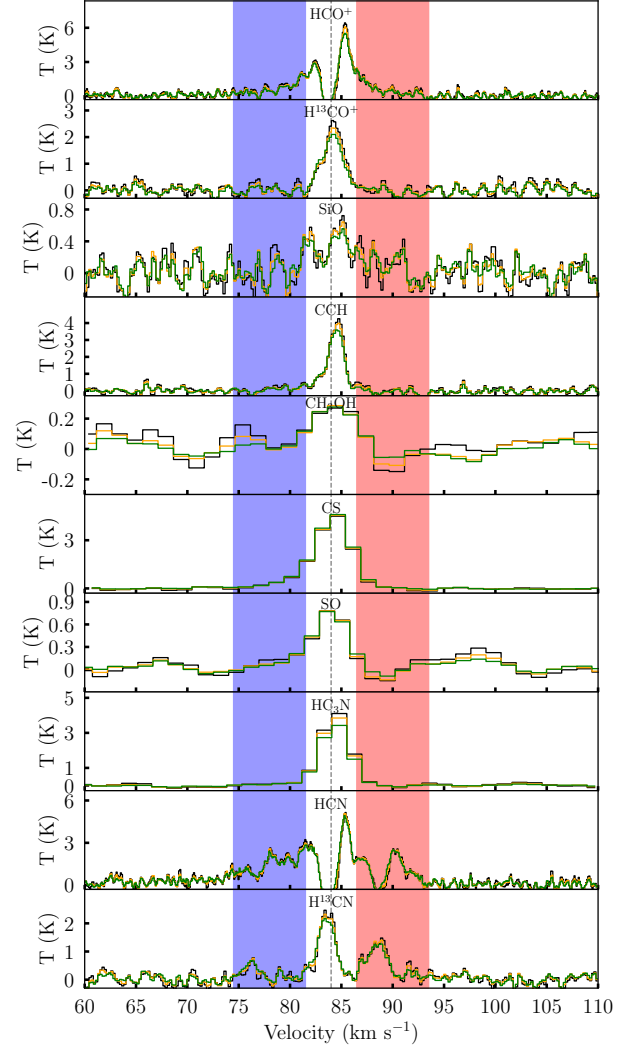


Figure F2. C4 ATOMS spectra. Similar to Fig. 4.

Table F1. Hi115 infall parameters.

Core	v_{infall}		σ		M_{infall}	
	HCO ⁺ km s ⁻¹	H ¹³ CO ⁺ km s ⁻¹	HCO ⁺ km s ⁻¹	H ¹³ CO ⁺ km s ⁻¹	HCO ⁺ M _⊙ kyr ⁻¹	H ¹³ CO ⁺ M _⊙ kyr ⁻¹
C2 ^(a)	0.58±0.02		0.43±0.03		2.7±1.1	
C3	1.07±0.05	0.51±0.05	0.87±0.03	0.62±0.02	5.4±2.1	2.6±1.5
C5	1.58±0.71	0.08±0.06	1.46±0.27	0.65±0.03	4.5±2.7	0.23±0.19

^(a) H¹³CO⁺ $J = 1 - 0$ profile of C2 does not have clearly blue asymmetry and therefore Hi115 modelling is not applied.

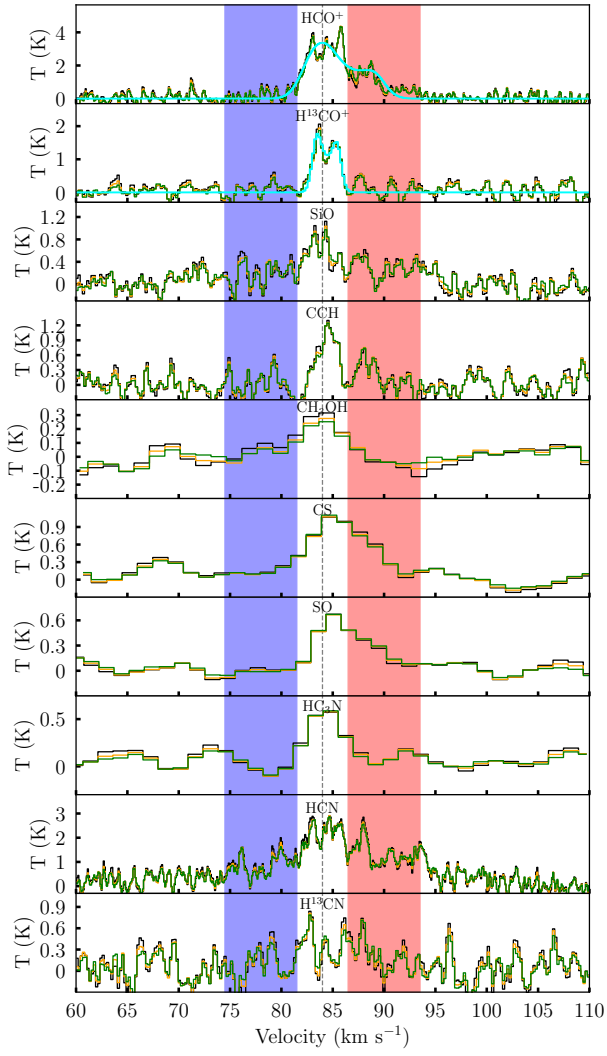


Figure F3. C5 ATOMS spectra. Similar to Fig. 5.

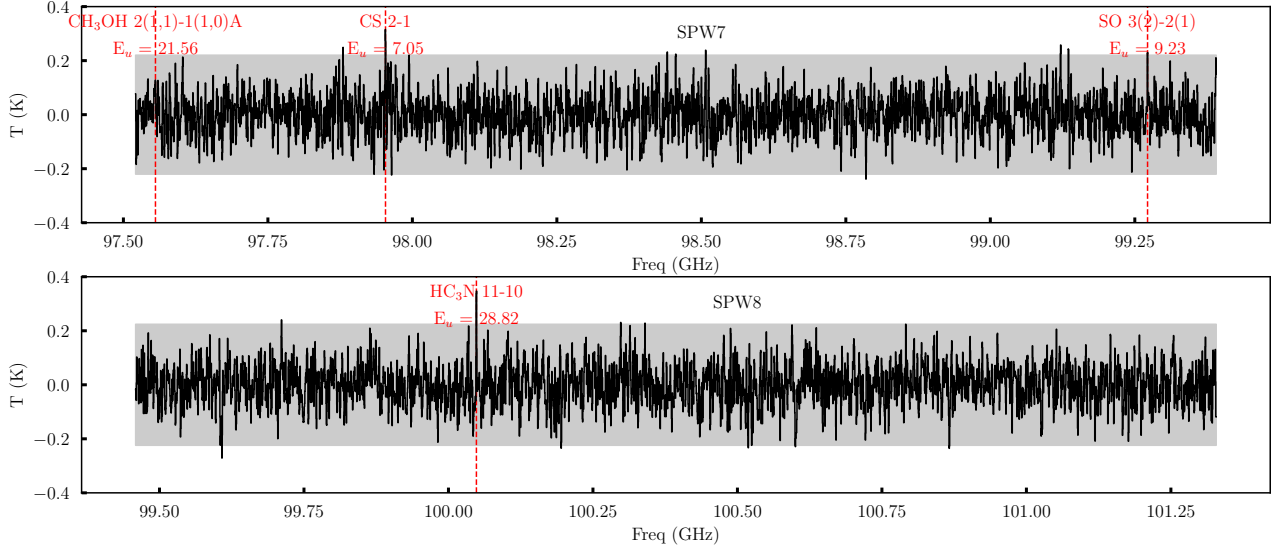


Figure F4. Core C2 ATOMS wide spectral windows SPW7 and SPW8. The gray shadows highlight the 3σ threshold. The red lines mark the spectra presented in Fig. 4.

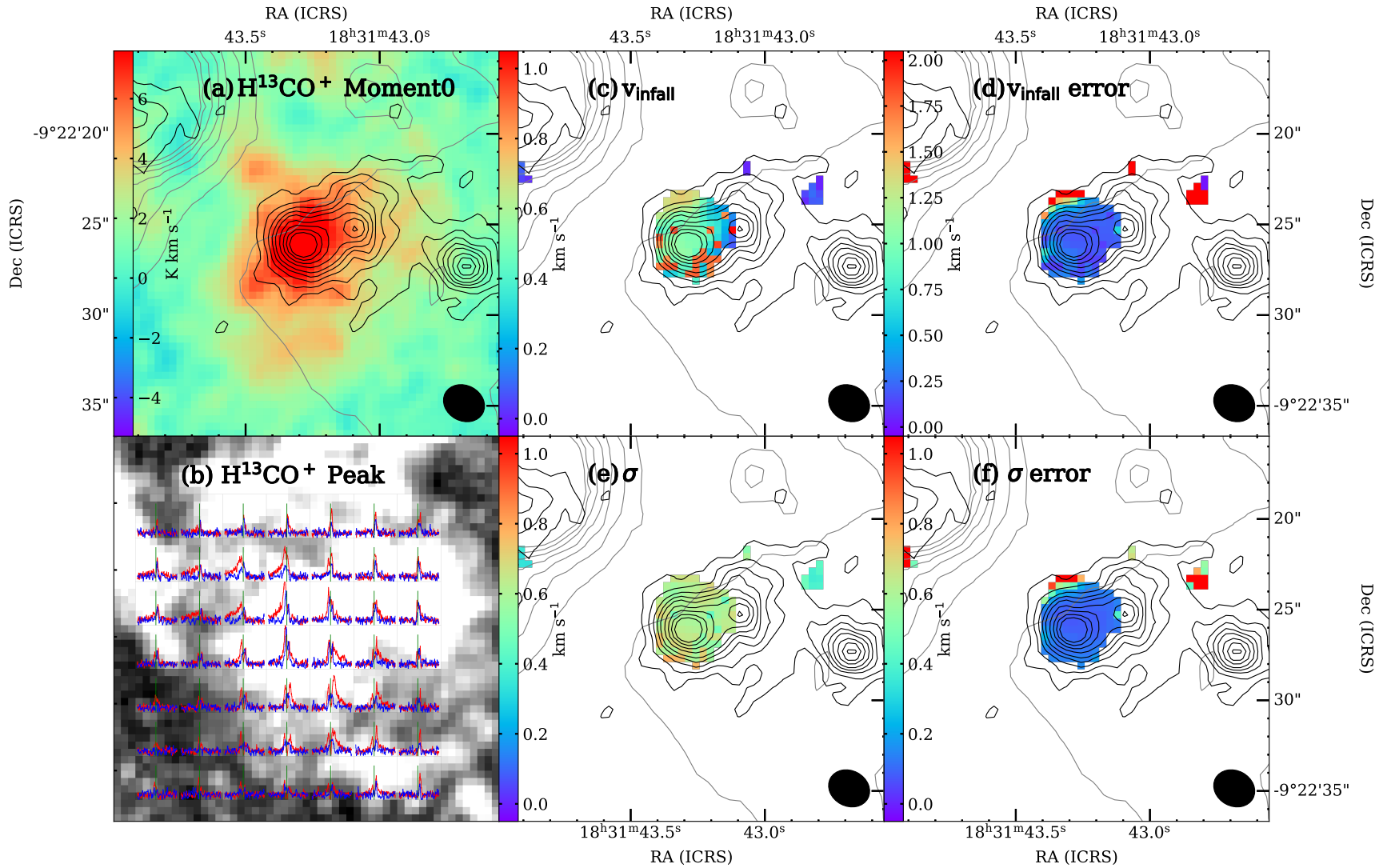


Figure F5. H^{13}CO^+ $J = 1 - 0$ infall parameters estimated by the Hi115 modelling. *Panel a:* H^{13}CO^+ $J = 1 - 0$ zeroth moment overlaid with the contours of $8\ \mu\text{m}$ (gray, the levels are the same as Fig. B1) and 3 mm emission (black, the levels are the same as Panel a of Fig. 3). The black ellipse represents the ATOMS beam. *Panel b:* H^{13}CO^+ line peak map overlaid with the grid spectra of HCO^+ $J = 1 - 0$ (red) and H^{13}CO^+ $J = 1 - 0$ (blue). *Panels c to f:* infall velocity, velocity dispersion and their errors derived from H^{13}CO^+ $J = 1 - 0$ with the Hi115 modelling.

APPENDIX G: PDR MOLECULES ANALYSES

G1 Structural similarity index measure

To compare the intensity spatial distributions between CCH $N_{J,F} = 1_{3/2,2} - 0_{1/2,1}$ and other lines, we make use of the SSIM method⁶ which is based on three comparison measurements between the samples' luminance, contrast, and structure (Wang et al. 2004). The ATOMS data cubes are smoothed to a common velocity resolution of 3 km s^{-1} (channel width is 1.5 km s^{-1}) for the SSIM calculations. Panels *a* to *i* of Fig. G2 show the channel-by-channel SSIM calculations for the ATOMS spectra, ranked from upper left to bottom right according to the maximum SSIM value of the maps. A larger value in the SSIM map means the emission spatial distributions are more similar. Panels *a* to *e* present a “bar” morphology with a slope of one, suggesting that there is a detectable similarity in emission spatial distribution between CCH $N_{J,F} = 1_{3/2,2} - 0_{1/2,1}$ and the referred lines. We classified these molecules as PDR tracers. Panels *f* to *i* have no significant structure and therefore these molecules do not trace the conspicuous PDR shown in CCH. We classified them as star formation tracers.

The zeroth moment maps for PDR tracers and star formation tracers are shown in the left and right panels of Fig. G1, respectively. NH_3 is also classified as the star formation tracer due to the lack of detection in the I18290 PDR.

G2 CCH velocity decomposition

To decompose the evaporative and compressed components, we fit the CCH $N_{J,F} = 1_{3/2,2} - 0_{1/2,1}$ PDR spine PV cut image position-by-position with double Gaussians using the MCMC. There are five parameters A_1 , A_2 , B_1 , $B_{21} = B_2 - B_1$, C_1 , and C_2 in the double-Gaussian model

$$\text{model} = A_1 \exp\left(-\frac{(v - B_1)^2}{2C_1^2}\right) + A_2 \exp\left(-\frac{(v - B_1 - B_{21})^2}{2C_2^2}\right). \quad (\text{G1})$$

In the MCMC modelling, we limit parameter space as follows:

- $A_1, A_2 > 0.4 \text{ K}$, to ensure SN ratio > 2 .
- $81 \text{ km s}^{-1} < B_1 < 87 \text{ km s}^{-1}$ and $1 \text{ km s}^{-1} < |B_{21}| < 4 \text{ km s}^{-1}$. Choice of the minimum $|B_{21}|$ is kind of arbitrary but reasonable according to Fig. G3.
- C_1 and C_2 , which represent the velocity dispersion, are required to be more than 0.4 km s^{-1} (width of two channels) and less than 0.8 km s^{-1} . The upper limit of 0.8 km s^{-1} , corresponding a FWHM of $\sim 1.9 \text{ km s}^{-1}$, is a reasonable value indicated by Fig. G3.

The modelled PV map and its residual are shown in Panels *b* and *c* of Fig. G3, respectively. The double-Gaussian model reconstructs the raw PV cut map very well, with a residual of $\sim 0.17 \text{ K}$.

Whether the PV cut map could be modelled by the single Gaussian is also tested. The single-Gaussian modelled PV and residual maps are shown in Panels *d* and *e* of Fig. G3, respectively. Several notable vertical strips indicated by the red arrows in the residual map imply the existence of the second component. The standard deviation ratios of single-Gaussian residual to double-Gaussian residual in each position show that the single-Gaussian model has a larger residual in most positions.

This paper has been typeset from a \LaTeX file prepared by the author.

⁶ https://scikit-image.org/docs/stable/api/skimage.metrics.html#skimage.metrics.structural_similarity

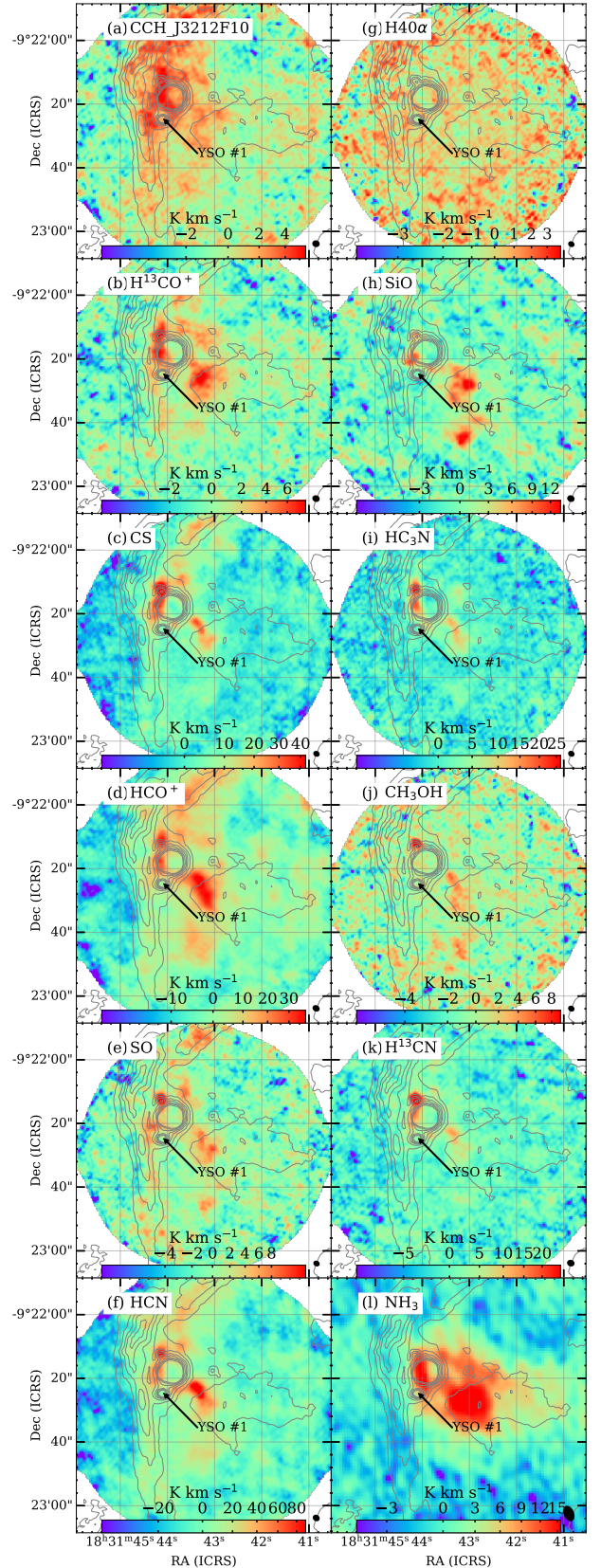


Figure G1. ATOMS spectra and VLA NH_3 (1,1) zeroth moment maps. The gray contours represent $8 \mu\text{m}$ emission with levels the same as the gray contours in Fig. B1. The arrow indicates the position of YSO #1. The left and right columns show the PDR tracers and star formation tracers, respectively.

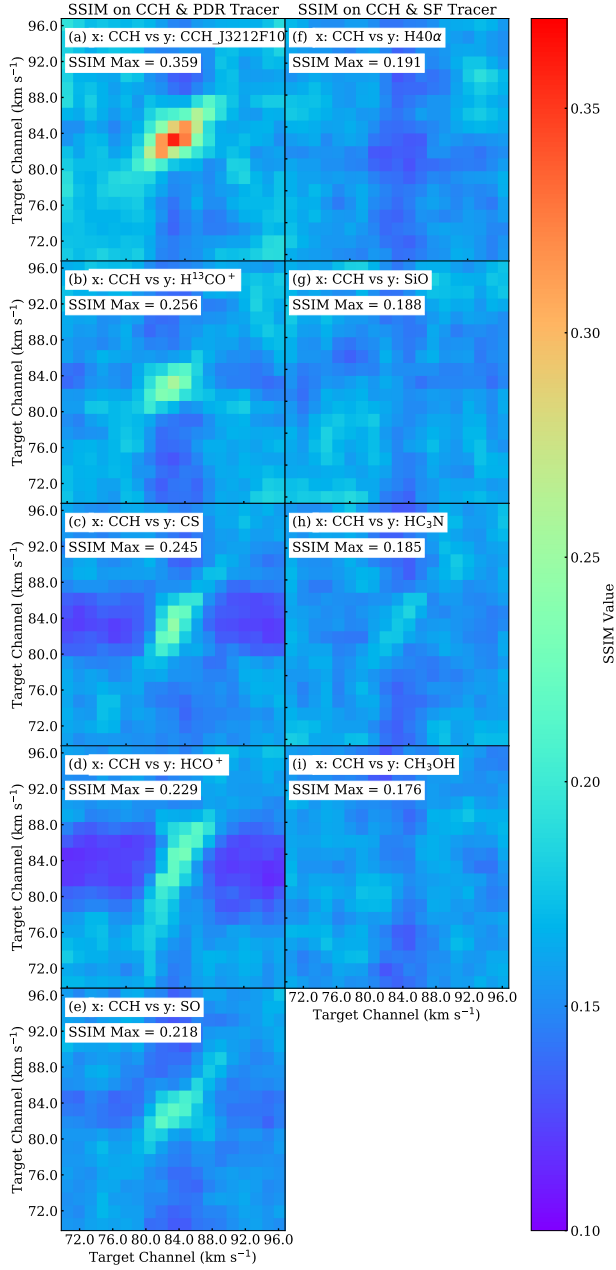


Figure G2. Structural similarity index measure (SSIM) tests with CCH $N_{J,F} = 1_{3/2,2} - 0_{1/2,1}$ emission. *Panel a* shows the SSIM test for CCH $N_{J,F} = 1_{3/2,2} - 0_{1/2,1}$ and CCH $N_{J,F} = 1_{3/2,1} - 0_{1/2,0}$. The left and right columns show the PDR and star formation tracers, respectively.

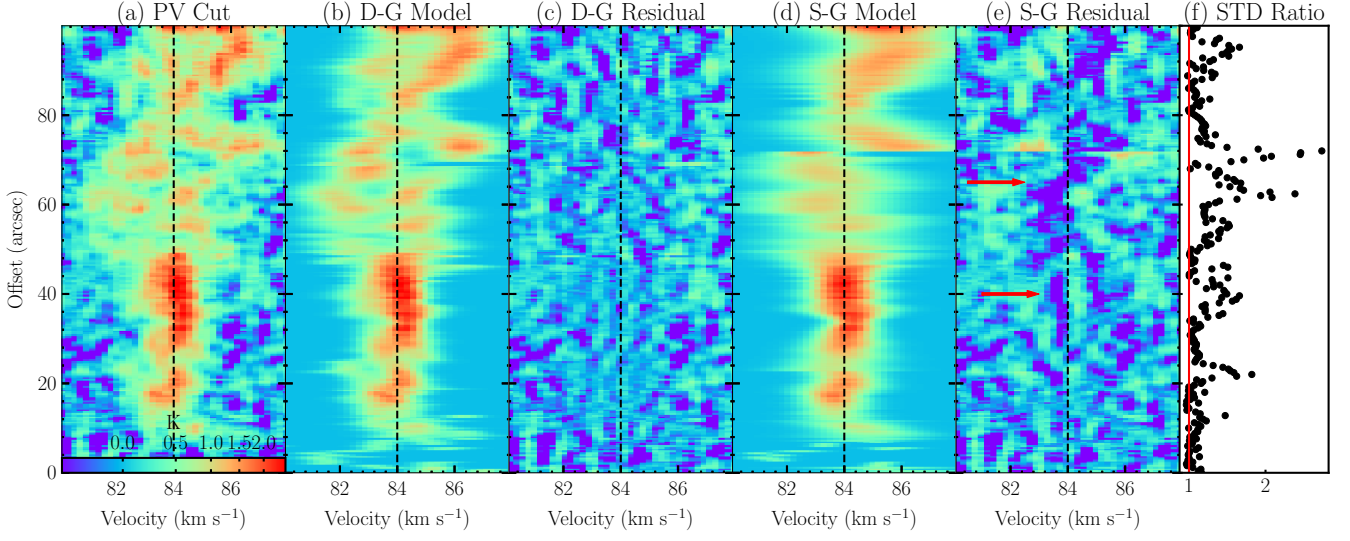


Figure G3. CCH $N_{J,F} = 1_{3/2,2} - 0_{1/2,1}$ PDR spine PV models. *Panel a:* PV cut along the $8\ \mu\text{m}$ spine. *Panels b and c:* Double-Gaussian position-by-position modelling result and its residual, respectively. *Panels d and e:* Single-Gaussian position-by-position modelling result and its residual, respectively. *Panel f:* Standard deviation ratio of the single Gaussian model residual-to-double Gaussian model residual at each position.

¹Kavli Institute for Astronomy and Astrophysics, Peking University, 5 Yiheyuan Road, Haidian District, Beijing 100871, China

²Shanghai Astronomical Observatory, Chinese Academy of Sciences, 80 Nandan Road, Shanghai 200030, China

³Key Laboratory for Research in Galaxies and Cosmology, Chinese Academy of Sciences, 80 Nandan Road, Shanghai 200030, China

⁴Aix Marseille Univ, CNRS, CNES, LAM, Marseille, France

⁵Institut Universitaire de France (IUF)

⁶Department of Physics, P.O. box 64, FI-00014, University of Helsinki, Finland

⁷Department of Astronomy, Yunnan University, Kunming, 650091, China

⁸Indian Institute of Space Science and Technology, Thiruvananthapuram 695 547, Kerala, India

⁹Departamento de Astronomía, Universidad de Concepción, Casilla 160-C, Concepción, Chile

¹⁰Max-Planck-Institute for Astronomy, Königstuhl 17, D-69117 Heidelberg, Germany

¹¹Departamento de Astronomía, Universidad de Chile, Las Condes, 7591245 Santiago, Chile

¹²Center for Astrophysics, Harvard & Smithsonian, Cambridge, MA, USA

¹³Jet Propulsion Laboratory, California Institute of Technology, 4800 Oak Grove Drive, Pasadena CA 91109, USA

¹⁴Korea Astronomy and Space Science Institute, 776 Daedeokdaero, Yuseong-gu, Daejeon 34055, Republic of Korea

¹⁵University of Science and Technology, Korea (UST), 217 Gajeong-ro, Yuseong-gu, Daejeon 34113, Republic of Korea

¹⁶Instituto de Radioastronomía y Astrofísica, Universidad Nacional Autónoma de México, Antigua Carretera a Pátzcuaro # 8701, Ex-Hda. San José de la Huerta, Morelia, Michoacán, México C.P. 58089

¹⁷Nobeyama Radio Observatory, National Astronomical Observatory of Japan, National Institutes of Natural Sciences, Nobeyama, Minamimaki, Minamisaku, Nagano 384-1305, Japan

¹⁸Department of Astronomical Science, The Graduate University for Advanced Studies, SOKENDAI, 2-21-1 Osawa, Mitaka, Tokyo 181-8588, Japan

¹⁹Department of Astronomy, School of Physics, Peking University, Beijing, 100871, China

²⁰National Astronomical Observatories, Chinese Academy of Sciences, Beijing 100101, China

²¹University of Chinese Academy of Sciences, Beijing 100049, China